ATP11B-related Mitochondrial Dysfunction Serves as an Early Alert of Alzheimer's Disease

Jiao Wang[1,10], Shibo Zhang[1,10], Qian Li[2,5,6,7,10], Ruiqi Sun[1,10], Wenxin Qi[1,10], Naijun Dong[1,10], Chengshang Lyu[3], Xiaoping Liu[3], Hao Wu[1], Jianxin Zhou[1], Hongwei Shi[1], Cuiping Liu[1], Junyi Zhuang[1], Peiru Wu[1], Lin Huang[1], Jintao Gong[2,5,6], Shuaijing Ma[2,5,6], Di Li[2,5,6], Xingyan An[1,5,6], Wanwei Zhao[1], Xuanting Liu[1], Qin Han[2,5,6], Rongjia Zhu[2,5,6], Shihua Wang[2,5,6], Hongling Li[2,5,6], Jing Li[2,5,6], Tieqiao Wen[1], Evelyne Bischof[8,9], Luonan Chen[3,4,*], and Robert Chunhua Zhao[1,2,5,6,*]

[1]Laboratory of Molecular Neural Biology, School of Life Sciences, Shanghai University, 99 Shang Da Road, Shanghai, 200444, China.

[2]Institute of Basic Medical Sciences Chinese Academy of Medical Sciences, School of Basic Medicine Peking Union Medical College, Beijing,100005, China.

[3]Key Laboratory of Systems Health Science of Zhejiang Province, School of Life Science, Hangzhou Institute for Advanced Study, University of Chinese Academy of Sciences, Hangzhou, 310024, China.

[4]Key Laboratory of Systems Biology, Shanghai Institute of Biochemistry and Cell Biology, Center for Excellence in Molecular Cell Science, Chinese Academy of Science, Shanghai, 200031, China.

[5]Center for Excellence in Tissue Engineering, Chinese Academy of Medical Sciences, Beijing, 100005, China.

[6]Beijing Key Laboratory of New Drug Development and Clinical Trial of Stem Cell Therapy (BZ0381), Beijing, 100005, China.

[7]Cell Energy Life Sciences Group Co. LTD, Qingdao, 266200, China.

[8]Department of Basic and Clinical Medicine, Shanghai University of Medicine and Health Sciences, Shanghai, 201318, China.

[9]Department of Medical Oncology, Renji Hospital, School of Medicine, Shanghai Jiao Tong University, Shanghai, 200240, China.

[10]These authors contributed equally: Jiao Wang, Shibo Zhang, Qian Li, Ruiqi Sun, Wenxin Qi, Naijun Dong.

***Correspondence:**

Robert Chunhua Zhao
Dongdan Santiao No. 5, Beijing 100005, China.
Tel/Fax: +86-10-65125311, email: zhaochunhua@ibms.pumc.edu.cn

Luonan Chen
Room 304, XiBao-DaLou, 320 YueYang Road, Shanghai 200031, China.
Tel: +86-21-5492-0100, Fax: +86-21-5492-0120, email: lnchen@sibs.ac.cn

Abstract

The progressive nature of Alzheimer's disease (AD) poses significant challenges in reversing cognitive decline and motor impairments once irrecoverable damage has occurred. This underscores the importance of prioritizing the development of strategies for early detection, prevention, and intervention. Here, we confirm mitochondrial dysfunction as a pivotal pre-disease indicator of AD, with 12 of 13 protein-encoding genes contributed by mitochondrial DNA and key nuclear genes required for the assembly and regulation of mitochondrial respiratory supercomplex showing early alterations. ATP11B, encoding a type IV P-type ATPase, was revealed as a tipping point gene at AD pre-disease stage and essential for maintaining mitochondrial integrity and energy homeostasis in major brain cell populations. ATP11B overexpression enhances cognitive performance in adult mice and an AD mouse model, providing substantial support for the proposition that mitochondrial dysfunction precedes AD pathology. This research positions ATP11B-indicated mitochondrial dysfunction as a potential biomarker for timely diagnosis of AD, contributing further insights to the understanding of early AD pathogenesis and offering a promising avenue for future therapeutic strategies.

Introduction

Alzheimer's disease (AD) is a progressive neurodegenerative disorder that begins with memory loss and may evolve to the loss of speech, social interaction, and mobility. The hallmarks of the AD brain include the overproduction of amyloid plaques (Aβ), the accumulation of tau neurofibrillary tangles, and neuronal degeneration. While it is possible to determine the levels of Aβ and tau in body fluid samples collected from living patients, the definitive diagnosis of AD still relies on antemortem and postmortem histological evaluations[1,2]. Moreover, the presence of atypical symptoms in AD often results in a delayed diagnosis[3], and the asymptomatic phase of the disease[4] poses a challenge in determining the optimum time for medical intervention. Meanwhile, the pathological mechanism that holds the most promising therapeutic potential has not yet been fully understood. Although the macroscopic alterations in the AD brain can be dissected into specific cellular and subcellular activities such as reduced synapse number and plasticity in cholinergic neurons[5], mitochondrial dysfunction[6], altered energy metabolism[7], and disrupted Ca^{2+} homeostasis[8], the early changes in different types of cells prior to the onset of AD remain under-investigated.

During the last decade, we proposed and developed the theory of dynamic network biomarker (DNB) that focuses on the identification of a set of molecules changing before the onset and during the progression of a disease[9]. The DNB concept offers great potential for determining the tipping point of a disease that marks the critical transition from the normal state to the disease state, and has been proved to be a useful tool for the prediction of complex diseases, such as diabetes and cancer, before they enter an irreversible disease state[10–12]. In this study, we first applied the DNB method to a clinical RNA sequencing (RNAseq) dataset and confirmed that the tipping point of AD onset is alerted by changes in mitochondria-related genes. By stepwise clustering of genes at this tipping point, we identified ATP11B, a member of the superfamily of flippases, the type IV P-type ATPases, as a hub gene that shows significant downregulation during the pre-disease stage of AD. We demonstrate that ATP11B expression level and related energy metabolism are the core indices of mitochondrial dysfunction manifesting synchronously across major brain cell types, which may enable a comprehensive understanding of AD pathogenesis, as well as suggest a potential biomarker for the early predication and prevention of AD onset.

Results

Alterations in mitochondrial proteins and ATP11B expression mark the pre-disease state of AD

To pinpoint the pre-disease state of AD, we analyzed the RNAseq data of human dorsal lateral prefrontal cortex (DLPFC) retrieved from the Religious Orders Study/Memory and Aging Project (ROSMAP)[13]. The subjects were classified into four groups as documented in the ROSMAP clinical codebook[14] to represent stages before and after AD develops (Supplementary Table 1). Employing the local DNB (l-DNB) methodology[15], we aimed to identify a stage when the critical genes show the most significant fluctuation, indicating the early warning signals of AD. The average DNB score of all the 15725 genes was observed with an upward trend at stage II (Supplementary Fig. 1a, global), suggesting that the genetic network began to exhibit instability as early as the subjects showed mild cognitive impairment. We then ranked the genes according to their DNB scores at stage II and defined the top 20 (<0.2%) genes with the highest scores as the dominant genes. The average DNB score of these genes reached its peak at stage II (Supplementary Fig. 1a, dominant group). This confirms stage II as the pre-disease phase of AD. It is of note that 19 of the 20 dominant genes were mitochondria-related genes, including 12 of the 13 protein-encoding genes contributed by mitochondrial DNA (mtDNA)[16] and key nuclear genes necessary for the assembly and functions of mitochondrial respiratory supercomplex, such as components of cytochrome c oxidase (COX) (Fig. 1a and Supplementary Table 2). Additionally, these proteins were enriched in pathways associated with AD including ATP metabolism and neurodegeneration (Fig. 1b). These observations suggest that mitochondria-related genes show early-warning alterations prior to the emergence of definitive AD symptoms.

To explore additional undiscovered genes that might warn of AD onset, we conducted multistep screenings on the initial 15725 genes. Considering that the dysregulation of axonal transport including mitochondrial trafficking and the compromise of plasma membrane integrity occur early in AD[17,18], we narrowed the scope of candidate genes by overlapping with members of plasma membrane proteins (GO:0005886) involved in transport (KW-0813) (Supplementary Fig. 1b). Among the 268 genes screened, we identified 48 differentially expressed genes (DEGs) by comparing stage I (healthy stage) to stage II (pre-disease stage). Then Mfuzz clustering was employed to separate these genes into two sub-clusters that showed upregulation and downregulation as AD progresses from stage I to stage V, respectively (Supplementary Fig. 1c). We hypothesized that the 37 genes in the sub-cluster with persistent downregulation were implicated in mitochondrial activities and performed a final screening by restricting their protein identities to translocases (KW-1278) and endoplasmic reticulum (ER) components (GO:0005783) (Supplementary Fig. 1d), which are two essential factors required for normal mitochondrial function[19,20]. This refined screening process resulted in 3 genes, among which we selected ATP11B for further study. On the one hand, decreases in the levels of most phospholipids in the brain were reported in AD[21]. On the other hand, ATP11B, a phospholipid flippase, has been shown to play an essential role in synaptic integrity and neurotransmitter release[22], which are dysregulated in AD[5,23]. Therefore, we speculate that ATP11B is a primary tipping point gene, with its declining expression signifying mitochondrial dysfunction and AD onset. Indeed, the protein-protein interaction (PPI) network, with ATP11B as the hub node, exhibited systematic instability starting from stage II (Fig. 1c). The genes within this network displayed distinct patterns of changes in expression and were classified into 4 clusters (Supplementary Fig. 2). It is noteworthy that ATP11B fell into cluster 1, which appeared to be associated with more disease pathways than any other cluster (Supplementary Fig. 2). Consistently, we found that the mRNA level of *ATP11B* in normal human DLPFC began to decline when the subjects were in their mid-20s (Fig. 1d). This aligns with the early-warning role of ATP11B expression for age-related chronic diseases, such as AD. Furthermore, in the hippocampus of AD patients, endogenous ATP11B colocalized strongly with Aβ plaques (Fig. 1e). In the hippocampus of acute AD mice, ATP11B colocalized with not only Aβ plaques but also microglia marker IBA1 (Fig. 1f). These findings point ATP11B to additional roles in AD pathology on top of its potential as an early indicator, including its possible involvement in the maintenance of Aβ homeostasis.

ATP11B deficiency induces cognitive defects and mitochondrial dysfunction

To further determine the physiological functions of ATP11B, we evaluated the phenotypes and cognitive performances of *Atp11b*$^{-/-}$ mice. Compared with wild-type littermates with a median survival time of 469 days, *Atp11b*$^{-/-}$ mice survived only 400.5 days on average (Fig. 2a). In the Morris water maze test, both young (3 months) and middle-aged (12 months) *Atp11b*$^{-/-}$ mice spent significantly more time finding the escape platform, compared with the wild-type controls (Fig. 2b). In addition, middle-aged *Atp11b*$^{-/-}$ mice spent significantly less time in the quadrant where the platform was located after it was removed (Fig. 2b). In the Y maze test, both young and middle-aged *Atp11b*$^{-/-}$ mice spent significantly less time staying in the new arm compared with the wild-type mice, while only young *Atp11b*$^{-/-}$ mice explored the new arm less frequently (Fig. 2c). Furthermore, in acute AD mice, the deposition of Aβ plaques and tau tangles in the brain was enhanced when *Atp11b* was knocked out (Fig. 2d). In memory evaluation tests, it took longer for acute AD mice with ATP11B deficiency to find the escape platform in the Morris water maze and these mice spent significantly less time exploring the new arm of the Y maze compared with normal acute AD mice (Fig. 2e, f). These results indicate that ATP11B deficiency leads to cognitive impairments in normal mice and exacerbates the symptoms of AD.

Given that a significant portion of AD-associated genes identified by l-DNB were related to mitochondrial functions, we examined key factors involved in mitochondrial quality control. Compared with wild-type mice, there were more mitochondria in pairs or clusters than individual mitochondria in the hippocampus of *Atp11b*$^{-/-}$ mice, and the number of cells with paired or clustered mitochondria was significantly increased (Fig. 2g). Concurrently, the levels of mitochondrial fusion mediators (MFN1, MFN2, OPA1) were significantly decreased and those of proteins promoting mitochondrial fission (DRP1, FIS1) were increased (Fig. 2h). Altered mitochondrial dynamics may impair the electron transport chain (ETC), and undermine ATP production, as suggested by the reduced ATP level in the hippocampus of *Atp11b*$^{-/-}$ mice (Fig. 2i). The decrease in ATP level may result from a shift in energy metabolic pathway from oxidative phosphorylation to anaerobic glycolysis, as evidenced by a rise in lactic acid level and an elevated ratio of lactic acid to pyruvic acid (Fig. 2j, k). Meanwhile, the expression of mitophagy mediators, PINK1, Parkin, and optineurin (OPTN), was significantly enhanced (Fig. 2h). This is likely an emergency measure for antagonizing the accumulation of dysfunctional mitochondria. Our results show that the function of ATP11B is indeed closely related to mitochondrial activities.

ATP11B deficiency alters cellular distribution, intercellular communication and memory-related genes in mouse hippocampus

To evaluate the effect of ATP11B deficiency on cellular activities, we performed single-cell RNAseq analysis on mouse hippocampus. The proportions of active neural stem cells (aNSCs), astrocytes, endothelial cells and mural cells were higher, and those of ependymal cells, neurons, and oligodendrocytes were lower in *Atp11b*$^{-/-}$ mouse hippocampus than in wild-type mouse hippocampus, while the percentages of microglia and T cells were almost identical in the two hippocampi (Fig. 3a, b). Further cell-cell communication analysis revealed that the number of intercellular interaction among different types of cells and the interaction strength were both weakened in *Atp11b*$^{-/-}$ mouse (Fig. 3c, d). This effect was especially pronounced in aNSCs, as their interaction with other cell populations was either diminished or lost (Fig. 3e). The disruption of intercellular communication may have a direct impact on cellular behavior, illustrated by the observed shift in the lineage commitment of aNSCs upon *Atp11b* knockout, resulting in less neurogenesis and more astrocytogenesis (Fig. 3f, g). Furthermore, the DEGs between these two hippocampi were found to be involved in cellular respiration and energy metabolism (Fig. 3h), which were particularly evident in neurons (Supplementary Fig. 3a). Correspondingly, the hub molecules in the PPI network of DEGs in either the entire mouse hippocampus or hippocampal neurons were implicated in mitochondrial functions (Fig. 3i, Supplementary Fig. 3b), such as the COX subunits. This reaffirms the involvement of ATP11B in mitochondrial activities.

To further verify the association of ATP11B with brain function, we performed spatial single-cell transcriptomics analysis. DEGs between brain sections of mice with or without *Atp11b* knockout were observed in 26 cell populations (Fig. 4a). Notably, the DEGs enriched in cell clusters representing the hippocampus (clusters 20 and 25) (Fig. 4b) were predominantly related to cognitive functions (Fig. 4c). Correspondingly, significant regulations of gene expression were observed in neurons and aNSCs with marginal regulation in microglia (Fig. 4d-f). These findings were in line with our RNAseq results showing significant alterations in the proportions of neurons and aNSCs in the hippocampus of *Atp11b*$^{-/-}$ mouse compared with wild-type littermates, while the microglia population remained largely unaffected. This local gene regulation in neurons and aNSCs might represent a temporary compensatory action to reprogram functional neural cells before irreversible damage is generated, which supports the warning role of ATP11B at the tipping point.

ATP11B maintains mitochondrial integrity and synaptic transmission in neuronal cells

As mitochondria-related proteins and pathways were dysregulated in response to ATP11B deficiency (Fig. 2h, Fig. 3h, i), we next attempted to identify mitochondrial activities primarily compromised. In neuronal cells, *ATP11B* knockdown led to a significant decrease in the activities of superoxide dismutase (SOD) and catalase (CAT) and a significant increase in H_2O_2 level (Fig. 5a), suggesting a cellular redox imbalance. Simultaneously, ATP production was reduced, corresponding to a rise in intracellular glucose level and an increased ratio of lactic acid to pyruvic acid (Fig. 5a). This could be a result of an imbalance in mitochondrial dynamics, indicated by diminished expression of *MFN1* and *MFN2*, and increased expression of *DRP1* and *FIS1* (Fig. 5b). Correspondingly, mitochondrial elongation was obviously reduced (Fig. 5c), accompanied by a decrease in mitochondrial membrane potential (MMP) (Fig. 5d) and an increase in the opening of mitochondrial permeability transition pore (mPTP) (Fig. 5e). Abnormal mPTP opening promotes the production of reactive oxygen species (ROS), and can also activate mitophagy[24]. Indeed, the primary mitophagy driver Parkin (encoded by *PRKN*) and the autophagosome marker LC3 were seen recruited to the mitochondria (Fig. 5f) and with enhanced expression in *ATP11B*-silenced neuronal cells (Fig. 5g). Meanwhile, the expression of other key mitophagy mediators including *PINK1*, *OPTN*, and *p62*, was also boosted (Fig. 5g). These results suggest that *ATP11B* knockdown in neuronal cells causes disturbances in mitochondrial quality control, represented by excessive fission and mitophagy.

The activation of sonic hedgehog (SHH) pathway shifts the energy-producing state of hippocampal neurons from anaerobic to aerobic[25]. Consistently, in *ATP11B*-silenced neuronal cells with a preference for anaerobic respiration, all components of the SHH pathway, including the ligand SHH, the receptor PTCH1, the signaling regulator smoothened (SMO) and the final transcriptional effector zinc finger protein GLI1, were suppressed (Fig. 5h). The suppression of SHH pathway was a contributing factor to excessive mitochondrial fission, as the inhibiting effect on DRP1 expression by purmorphamine, an SHH pathway agonist, was reversed by *ATP11B* knockdown (Fig. 5i). Meanwhile, the level of DRP1 phosphorylation at Serine 637, which inhibits its oligomerization and subsequent mitochondrial fission[26], was significantly reduced in *ATP11B*-silenced neuronal cells (Fig. 5h). Intriguingly, DRP1 was found physically associated with GLI1 and their interaction was compromised upon the silencing of *ATP11B* (Fig. 5j). These results indicate that ATP11B plays a protective role in neurons against energy disequilibrium by maintaining SHH signaling pathway.

Next, we assessed whether defective mitochondria resulting from ATP11B deficiency affect high energy-demanding synapses. In the hippocampal neurons of *Atp11b*$^{-/-}$ mice, the thickness of the postsynaptic density (PSD) and the curvature of the synaptic interface were diminished, while the synaptic cleft width was increased (Fig. 5k), indicating a significant remodeling of synaptic structure[22]. Further electrophysiological evaluation revealed that, under a series of current stimuli, the excitability of CA1 neurons in *Atp11b*$^{-/-}$ mice was significantly reduced compared with wild-type mice, represented by decreased firing frequency despite higher peak action potentials (Fig. 5l). Importantly, both the frequency and amplitude of miniature excitatory postsynaptic currents (mEPSCs) of CA1 neurons were significantly lower in *Atp11b*$^{-/-}$ mice than those in wild-type mice (Fig. 5l). We then focused on α-amino-3-hydroxy-5-methyl-4-isoxazolepropionic acid receptor (AMPAR), a glutamate receptor that mediates excitatory synaptic transmission and the synaptic trafficking of which is required to retain memory in mice[27]. In both *ATP11B*-silenced neuronal cells and the hippocampus of *Atp11b*$^{-/-}$ mice, the expression of GRIA1 and GRIA2, the most abundant subunits of AMPAR in the hippocampus, was significantly downregulated compared with their respective controls (Supplementary Fig. 4a, b). Furthermore, the levels of GRIA1 and GRIA2 in the plasma membrane and the synaptosomes were concurrently downregulated in *Atp11b*$^{-/-}$ mouse hippocampus, while their levels in the cytoplasm remained unaffected (Supplementary Fig. 4c, d). This indicates that ATP11B deficiency interferes with the proper incorporation of AMPAR into synapses.

ATP11B deficiency induces over-inflammation and impairs microglial phagocytosis

While *Atp11b* knockout minimally affected the number of microglia in mouse hippocampus, it altered microglia-mediated pathway, as evidenced by changes in molecules in response to interferon-γ (Fig. 6a). Compared with the wild-type mice, the microglia in the hippocampus of *Atp11b*$^{-/-}$ mice, had significantly more and longer branches (Fig. 6b), a characteristic that may indicate a transitional "alert" state before microglia become fully activated[28]. Microglia with hyper-ramified or bushy morphology are thought to represent the early stage of inflammatory responses[28,29]. This is supported by our observation that the levels of pro-inflammatory cytokines interleukin-1β (IL-1β), interleukin-6 (IL-6) or tumor necrosis factor alpha (TNF-α) were significantly higher in *Atp11b*-silenced microglial cells and the cortex of *Atp11b*$^{-/-}$ mice compared with the controls (Fig. 6c, Supplementary Fig. 5a). This effect was obviously enhanced and extended to the hippocampus when the mice were injected with lipopolysaccharide (LPS) (Supplementary Fig. 5a), a measure inducing chronic neuroinflammation[30]. The signaling pathway controlling the production of IL-1β, IL-6, and TNF-α was also augmented, represented by the up-regulation of Toll-like receptor *Tlr4* and the subunits (*Rela* and *Relb*) of nuclear factor kappa-light-chain-enhancer of activated B cells (NF-κB) (Supplementary Fig. 5b). In addition, the expression levels of microglial surface protein *Cd40* and inducible nitric-oxide synthase (iNOS, encoded by *Nos2*), both markers of pro-inflammatory M1 microglia[31], were higher in the hippocampus of *Atp11b*$^{-/-}$ mice compared with wild-type mice (Supplementary Fig. 5c). Consistently, the expression of iNOS and cyclooxygenase-2 (COX2), another marker of microglial activation[30], was enhanced in cultured microglial cells upon *Atp11b* knockdown (Supplementary Fig. 5d).

The excessive inflammation of microglia may be caused by oxidative stress[32]. Indeed, the intracellular ROS level was significantly increased accompanied with decreased SOD activity and reduced ATP level in *Atp11b*-silenced microglial cells (Fig. 6d, e). This may be attributed to the leakage of ROS from damaged mitochondria, as the MMP was significantly diminished (Fig. 6f), potentially resulting from excessive mPTP opening (Fig. 6g). Further analysis revealed an enhanced glucose intake in *Atp11b*-silenced microglial cells (Supplementary Fig. 6a), supported by boosted expression of two key glucose transporters in microglia *Glut1* and *Glut3*[33,34], while the level of the fructose transporter *Glut5* remained unchanged (Supplementary Fig. 6b). Accordingly, the level of pyruvic acid was increased (Supplementary Fig. 6c), majorly used for anaerobic aspiration, as indicated by an elevated level of lactic acid (Supplementary Fig. 6d). This metabolic switch is a signature of microglial activation[35,36], and mediated by mitochondrial fission[37], which is in line with our observation of increased mitochondrial mass in *Atp11b*-silenced microglial cells (Fig. 6h).

Considering that ATP11B is colocalized with Aβ and IBA1 in acute AD mice, we then examined the effects of ATP11B deficiency on the phagocytosis capacity of microglia. When

Atp11b was silenced, the proportion of microglial cells phagocytizing either Aβ or fluorescent microspheres was significantly decreased compared with the control cells (Fig. 6i). Further exploration demonstrated that the reduced capacity of phagocytosis in *Atp11b*-silenced microglial cells might be associated with lysosomal dysfunction, as damaged lysosomes were unrepairable shown by the accumulation of Galectin-3 and LC3 (Supplementary Fig. 6e). Moreover, the phagocytic defects may also be contributed by the intracellular accumulation of lipid droplets (Supplementary Fig. 6f), which accounts for the proinflammatory state in aging brain and AD brain[38,39].

ATP11B is involved in the neuronal lineage commitment of neural stem cells (NSCs)

Based on our observation of reduced neurogenesis (Fig.3b, g) and altered gliogenesis pathway (Fig. 7a) in the hippocampus of *Atp11b*$^{-/-}$ mouse, we further explored the effects of ATP11B deficiency on the stemness of aNSCs. In NSCs cultured *in vitro*, we found that the expression level of sex determining region Y-box 2 (*Sox2*), an important regulator of NSCs multipotency, was positively correlated with that of *Atp11b* (Fig. 7b). When *Atp11b* was knocked down, the total expression level of *Sox2* was decreased, with a reduction in the nucleus and an increase in the cytoplasm (Fig. 7c). Previous studies have reported that the binding of SOX2 to the promoters of proneural and neurogenic genes primes NSCs towards the lineage of neuronal progenitors but inhibits the initiation of neurogenesis[40,41], while the activation of canonical Wnt/β-catenin signaling leads to the nuclear translocation of β-catenin, lifting the suppression of SOX2 on proneural genes[42]. In *Atp11b*-silenced NSCs, increases in β-catenin expression and nuclear translocation were observed (Fig. 7d, e). This might indicate an emergency response against the cytoplasmic sequestration of SOX2, which has been suggested to negatively affect its activity[43]. Furthermore, DEGs in hippocampal aNSCs between *Atp11b*$^{-/-}$ and wild-type mice were found enriched in the ERK1/2 signaling pathway (Fig. 7a). Consistently, the ERK1/2 cascade was boosted in *Atp11b*-silenced NSCs, shown by more phosphorylated ERK1/2 (Fig. 7e) and the suppression of its negative feedback regulator dual-specificity phosphatase 6 (DUSP6[44], Fig. 7e). Moreover, the retention of SOX2 in the cytoplasm was likely due to a failure of energy supply, as the ATP level was significantly diminished in response to *Atp11b* knockdown (Fig. 7f), which was attributed to the switch to the lactic acid system for energy generation (Fig. 7g). This preference for anaerobic glycolysis might be a result of mitochondrial dysfunction, characterized by excessive fission (Fig. 7h, i) and aberrant opening of mPTP (Fig. 7j).

To explore the potential involvement of ATP11B in the transcriptional activity of SOX2, we performed chromatin immunoprecipitation-quantitative polymerase chain reaction (ChIP-qPCR) experiments. Remarkably, we found that SOX2 directly bound to the promoter region of *Atp11b* (Fig. 7k), and activated its transcription by suppressing repressive histone modifications, as indicated by an increase in H3K27me3 enrichment in the promoter region of *Atp11b* upon *Sox2* knockdown in NSCs (Fig. 7k). This observation implies a bidirectional regulatory relationship between SOX2 and ATP11B.

ATP11B overexpression rescues cognitive deficits

To confirm the cerebroprotective effects of ATP11B, we established a transgenic mouse model with neural-specific overexpression of ATP11B (Tg-*ATP11B*, Nestin-Cre). Significant differences in cognitive performance between Tg-*ATP11B* mice and wile-type controls were observed when the mice reached 12 months (Fig. 8a, b), an age when naturally aging mice begin to show memory impairments[45]. Specifically, in the Morris water maze test, even though the time spent finding the escape platform by these two groups of mice was comparable, middle-aged (12 months) Tg-*ATP11B* mice spent significantly more time in the quadrant where the platform was located after it was removed (Fig. 8a). In the Y maze test, middle-aged Tg-*ATP11B* mice spent similar time staying in the new arm but explored more frequently compared with their wild-type littermates (Fig. 8b). Furthermore, transient overexpression of ATP11B in the hippocampus led to enhanced spatial memory in 3xTg-AD mice, as evidenced by a reduced latency of the first platform crossover and an increased frequency of platform crossovers in the water maze (Fig. 8c). Interestingly, the rescuing effects of ATP11B were not seen in older 3xTg-AD mice (Fig. 8c). Younger 3xTg-AD mice with overexpressed ATP11B also exhibited improved working memory shown by a higher alternation percentage in the Y maze (Fig. 8d), and less anxiety indicated by a longer moving distance in the central area of an open field (Fig. 8e). Taken together, these findings suggest that ATP11B plays a protective role in the early stages of brain function impairments, aligning with its potential to signal the pre-disease state of AD.

Discussion

In this study, we identify mitochondria-related changes as the alerting signal for AD onset along with a hub gene ATP11B that shows declined expression as early as the subjects exhibit mild cognitive impairment, a prodromal stage proposed for AD[46]. The intrinsic functions of ATP11B are found to be a “safeguard” for mitochondrial integrity across three major cell populations in the brain (Fig. 9). This crucial role is closely linked to the core functions of these cells including synaptic transmission in neurons, inflammation activation by microglia and neurogenesis of aNSCs, in keeping with the significance of mitochondria in signifying the tipping point of AD.

Mitochondrial dysfunction has been considered as an early event in AD pathogenesis[47–49] that may precede Aβ deposition and tau pathology[50]. We for the first time report that almost all the proteins encoded by mtDNA show changes before AD-specific symptoms appear. This is in line with a previous study showing that the copy number of mtDNA was significantly lowered in the DLPFC of AD subjects, but not in the cerebellum which may show pathological changes later[51]. Besides mtDNA that encodes the functional subunits of mitochondrial complexes, the dominant genes identified by l-DNB also include nuclear genes encoding the structural and regulatory subunits, exampled by COX[52]. Among them, COX8A expression was significantly downregulated in the early affected brain regions (hippocampus and entorhinal cortex) of AD patients, and the frequencies of COX10 SNPs differed significantly between AD patients and controls in Chinese Han populations[53]. Our findings address the possibility that the overall mitochondrial health collapses systematically at the tipping point of AD onset.

Through a multistep clustering-identified gene, ATP11B, we demonstrate that altered energy metabolic pathway may synchronously occur in multiple cell types and is therefore a prerequisite index of mitochondrial dysfunction. Glucose hypometabolism, an early biomarker of AD[54–56], is reflected by our observations of reduced ATP levels and preference for anaerobic glycolysis in mouse hippocampus and three types of brain cells with ATP11B deficiency.

In high energy-demanding neurons, insufficient energy supply impairs synaptic activity, since every step of synaptic transmission requires ATP, such as the propagation of action potentials and synaptic vesicle cycling[57–59]. Our results contribute additional evidence, indicated by a decrease in AMPAR trafficking to the synaptosomes of *Atp11b*$^{-/-}$ mouse hippocampus. This may lead to the compromise of postsynaptic glutamatergic transmission[60], in line with our observation of reduced frequency and amplitude of mEPSCs in CA1 neurons. We verify that the change of energy metabolism induced by ATP11B deficiency in neurons is a result of mitochondrial abnormality attributed to the upregulation of DRP1 and the suppression of the SHH pathway. DRP1 is an important indicator of mitochondrial quality due to its roles in mitochondrial fission and mitophagy. While the stimulation of SHH signaling by recombinant SHH can restore mitochondrial health via the suppression of DRP1 expression[61], the application of bioactive SHH may reduce DRP1-mediated mitochondrial fission by decreasing DRP1 phosphorylation at serine 616[25]. Consistent with these findings, we reveal that the suppression of SHH pathway following *ATP11B* silencing promotes mitochondrial fission by upregulating the expression of DRP1 and reducing its phosphorylation at serine 637. Importantly, we show for the first time that this ATP11B-mediated intersection between the SHH pathway and mitochondrial fission appears to be independent of GLI1-mediated transcription, but through the direct interaction between GLI1 and DRP1.

Microglia, as the innate immune cells in the brain, require rapid energy supply to mediate cytokine secretion, chemotaxis and phagocytosis. A decline in ATP level as a reaction to *Atp11b* knockdown directly leads to reduced phagocytic activities in microglial cells. We and others[37] show that excessive mitochondrial fission is the underlying cause of ATP shortage and the metabolic pathway shift from oxidative phosphorylation to anaerobic glycolysis, which occurs early in AD[62]. The increased dysfunctional mitochondria may be released from microglia, transfer the injury to astrocytes and then to neurons, acting as a neurotoxic signal[63]. Also, lactate is reported to induce the release of proinflammatory cytokines (TNF-α, IL-6 and IL-1β) in microglia-enriched primary culture[64], as observed in *Atp11b*-silenced microglia cultured *in vitro*. Consistently, the upregulation of GLUT1 and GLUT3 may indicate the metabolic reprogramming of microglia and correlate with neuroinflammatory conditions[33,34]. Therefore, ATP11B deficiency-induced mitochondrial defects in microglia appear to induce a series of metabolic imbalance events, which can be considered as an early warning signal of immune dysregulation and a contributing factor to neurodegeneration in AD.

Quiescent NSCs have a low energy demand and mainly turn to anaerobic glycolysis for energy supply[65,66]. During the differentiation of NSCs, mitochondrial biogenesis, mtDNA copy number and aerobic metabolism are enhanced[67]. However, the preference of anaerobic glycolysis by *Atp11b*-silenced NSCs is not a representation of converting to a dormant state, as the stemness marker SOX2 displays downregulated expression and failure of nuclear import. The boost in ERK1/2 signaling may enhance astrocytogenesis[68], which is supported by our observation of a deviated lineage of aNSCs towards astrocytes in *Atp11b*$^{-/-}$ mouse hippocampus. In *ATP11B*-silenced NSCs, the nuclear translocation of β-catenin and the cytoplasmic sequestration of SOX2 dampen the chance of their interaction and may therefore curb the transcription of proneural genes. As ERK1/2 has been proposed to be the gatekeeper for NSCs to maintain self-renewal instead of neuronal differentiation[69,70], and may intersect with differentiation-promoting Wnt/β-catenin pathway[71], we propose that ATP11B is required for the initiation of neurogenesis. This notion is further validated with the finding of *ATP11B* transcription being mediated by SOX2. It can be speculated that lack of ATP11B leads to defective mitochondria and thus insufficient ATP necessary for the nuclear import of SOX2, while the subsequent failure of *Atp11b* transcription further exhausts the energy supply and SOX2 in the nucleus, both essential for neurogenesis.

The concurrent changes in mitochondrial function and energy metabolism in neurons, microglia and NSCs point to the possibility that different types of cells share a common mechanism of dysfunction preceding the disease onset. These cell types could be damaged earlier and more profoundly than others, as supported by a recent study showing that the neural transiently amplifying progenitor cells and microglia are the most affected cell populations by aging in primate hippocampus, which directly contributes to reduced neurogenesis and enhanced pro-inflammatory responses in aged brain[72].

Altogether, our findings shed light on an essential indicator of AD pre-disease stage, mitochondrial dysfunction, which can be indicated by ATP11B expression. The downregulation of ATP11B initiates early warning signals, evident through abnormal mitochondrial behaviors and altered energy metabolism across major cell populations in the brain. Significantly, our results provide support for the proposition that mitochondrial dysfunction precedes the development of AD pathology. This insight paves the way for novel therapeutic interventions targeting the restoration of mitochondrial function systematically as a strategy to prevent or delay the progression of AD.

Materials and methods

Animals

All animals were treated in accordance with the International Guidelines for Animal Research, and the animal protocols were approved by the Animal Ethics Committee of Shanghai University (Approval No. ECSHU 2021-039, date: March 26, 2021). Mice were kept on a 12/12 h light/dark cycle, at a constant temperature (22±1°C) and humidity (60–80%), with food and water *ad libitum*.

Atp11b$^{-/-}$ mice were constructed with the CRISPR technology by excising exons 13-15 of the *Atp11b* gene and introducing a shift mutation in the protein coding region (Beijing Viewsolid Biotech Co., Ltd).

Acute AD mice were generated by bilaterally injecting TAMRA-Amyloid-β (1-42) (Aβ_{1-42}, Best Biochem) into the hippocampus (anterior-posterior=1.95mm, medial-lateral=1.5mm, dorsal-ventral=-1.85mm).

The ATP11B transgenic mouse model (Tg-*ATP11B*) was constructed through the CRISPR/cas9 knock-in technique (Cyagen Biosciences Inc.) The Nes-2A-CreERT2 mice were purchased from Shanghai Model Organisms Center, Inc. To generate mice with neural-specific overexpression of ATP11B (Tg-*ATP11B*, Nestin-Cre), homozygous Tg-*ATP11B* mice were bred with Nes-2A-CreERT2 mice. For simplicity, mice denoted as Tg-*ATP11B* in the behavioral studies refer to mice with the neural expression of ATP11B.

3xTg-AD mice were purchased from Cavens Co. Ltd. For the overexpression of ATP11B in these mice, pLenO-RTP-CMV-ATP11B-EF1α-RFP-Puro lentivirus was bilaterally injected in the hippocampus (anterior-posterior=1.95mm, medial-lateral=1.5mm, dorsal-ventral=-

1.85mm).

Both male and female mice were used for experiments. For behavioral experiments, *Atp11b*$^{-/-}$ mice and acute AD mice of 3 months and 12 months, Tg-*ATP11B* mice of 6 months and 12 months, 3xTg-AD mice of 5 months and 12 months were used.

Cell lines

The human SH-SY5Y neuroblastoma cell line, the mouse BV2 cell line and the mouse C17.2 cell line were used as cellular models of neuronal cells, microglial cells, and neural stem cells, respectively. All types of cells were grown in DMEM containing 10%FBS and 1xPenicillin-Streptomycin at 37°C with 5% CO_2.

For the knockdown of *ATP11B*/*Atp11b*, cells were transfected with specific siRNAs using lipofectamine 2000. Negative control siRNAs were used for the control cells.

Classification of an AD RNAseq dataset

The bulk RNA-seq data used for analyzing the tipping point of AD were originally derived from ROSMAP[13] and downloaded from the AMP-AD Knowledge Portal (https://www.synapse.org/#WSynapse:syn2580853). The RNAs in the dataset were sequenced from the gray matter of human DLPFC[13]. A total of 443 subjects were selected and classified according to the final consensus cognitive status (the COGDX score) as I) NCI: no cognitive impairment (CI) (n=140), II) MCI: mild CI with no other cause of CI (n=112), III) MCI+, MCI with another condition causing CI (n=6), IV) AD: Alzheimer's, without any other cause of CI (n=155), V) AD+: Alzheimer' s with other medical condition(s) causing CI (n=18) and VI) other dementia: dementia due to other causes, no clinical evidence of AD (n=12). For the DNB analysis, the III and VI groups were excluded due to limited sample size and irrelevance to AD respectively. For all samples, the data of non-coding RNAs were removed and a total of 15725 transcripts remained for subsequent analysis.

DNB analysis

The l-DNB method used for the identification of the pre-disease stage of AD was described previously[15]. Briefly, the PPI network for each gene in the RNAseq dataset was constructed using StringDB (https://string-db.org, version 11.5) with a threshold score of ≥0.8. A single gene and its first-order neighbors were defined as the "in" group for this gene. The Pearson's correlation coefficient (PCC) of expression levels was calculated for each gene and any other genes. Then, three parameters were generated: SD_{in}, the standard deviation of expression levels of genes within an "in" group; PCC_{in}, the average PCC of expression levels between each gene and any other genes in its "in" group; PCC_{out}, the average PCC of expression levels between each gene and any other genes outside its “in” group. The DNB score was defined as $s = \frac{SD_{in} \times PCC_{in}}{PCC_{out}}$ and was calculated for each gene at each stage. The NumPy and Pandas packages of Python were used to analyze and calculate DNB scores.

Mfuzz clustering

The expression levels of each gene at each stage were averaged and transformed to z scores. Genes with distinct expression trends as AD progresses were sub-grouped via Mfuzz (version 2.56.0)[73] with the number of clusters being set at 2.

Behavioral evaluation

Before each behavioral experiment, the mice were acclimatized to the behavioral test room for 2-3 days.

Morris water maze test. The water tank was 150 cm in diameter and was divided into 4 quadrants. Titanium dioxide was added to the water to facilitate the recognition of the animals. A 10-cm platform was placed in the center of one fixed quadrant, 0.5 cm above the surface of the water. On Day 1, each mouse was placed in the water facing the tank wall at random positions. The time spent by the mice to locate the platform was recorded. Mice that did not find the platform within 60 s were manually guided onto it and were allowed to stay for 30 s. On Day 2-5, the platform was lowered to 0.7 cm below the surface of the water. Each mouse was placed into the water for 4 trials at different positions with intervals of 10 min. The time it took for the mice to reach the hidden platform was recorded. The maximum test time was set at 60 s. On Day 6, the platform was removed, and each mouse was allowed to freely explore the tank for 5 min. The time spent by the mice in the quadrant where the platform was located was recorded.

Y maze test. The Y-maze comprises of three plastic arms, each positioned at an angle of 120° from another, with dimensions of 50 cm in length, 10 cm in width, and 35 cm in height. The three arms of the Y-maze were randomly designated as: the starting arm, the other arm, and the new arm. After the acclimatization, each mouse was placed in the distal part of the starting arm and allowed to explore freely for 5 min. The number of all arm entries and alternations were recorded. Then the new arm was obstructed with an opaque partition, while the starting arm and the other arm were left open. Each mouse was allowed to explore freely for 5 min. Subsequently, the partition was removed, and each mouse was allowed to explore freely for another 5 min. The frequency of entering the new arm and the duration in the new arm were recorded. The apparatus was cleaned with 70% ethanol between test runs to remove odor interference.

Open field test. The open field apparatus is a coverless box measuring 40 cm in length, 40 cm in width and 30 cm in height. Each mouse was placed in the middle of the apparatus and was allowed to explore freely for 10 min. The total distance traveled and the moving distance in the central region of the apparatus were recorded.

PET/CT

PET/CT experiments were performed using a Siemens Inveon PET/CT system according to the standard protocols and procedures[74]. Briefly, mice were anesthetized with isoflurane and radioactive probes for Aβ or tau ([^{18}F]-AV45 or [^{18}F]-PBB3, 0.5 mCi) were administered by tail vein injection. After 50 min, PET/CT images were acquired over a 10-min duration.

Transcriptomics data of normal human DLPFC

The transcriptomics database of normal human DLPFC used in this study (https://maayanlab.cloud/DLPFC) provides data of genome-wide gene expression in the DLPFC of 69 healthy human subjects with the age ranging from 39 days to 49.5 years. The raw transcriptomics data were transformed to z scores to represent RNA levels.

Single-cell RNA sequencing (scRNA-seq)

Data processing. Raw scRNA-seq reads were processed with the Cell Ranger software (version 2.1.0) for sample demultiplexing, barcode processing, and genome mapping. Briefly, raw sequencing reads were mapped according to the mouse reference genome (GRCm39) using the STAR software (version 2.7.10a) with default parameters. Then the unique molecular identifiers (UMIs) were counted in each cell. Cells were regarded as of low quality if their total UMI counts or the number of genes detected (in log10 scale) were less than the median value of all cells minus three times the median absolute deviation. Additionally, cells were also excluded if the proportion of mitochondrial genes was larger than the median value of all cells minus three times the median absolute deviation. The Seurat R package (version 4.0) was applied in the quality control procedure.

Cell doublet detection and removal. The Scrublet (version 0.1) software was used to detect potential doublets in the scRNA-seq dataset. The threshold of doublet score was calculated with the bimodal distribution to identify microfluidic droplets that contained two or more cells. Cells with a doublet score lower than the threshold were removed.

Data integration of all samples. After removing low-quality and doublet cells, the remaining cells in all samples were subjected to normalization and integration. The RNA expression level in each cell was normalized against the total RNA expression level in all cells by utilizing the LogNormalize function integrated in the Seurat package. Normalized expression counts were then multiplied by a scale factor (10,000 in our case) and log-transformed. The normalized gene expression matrix was adopted to select the top 2000 variable genes with an appropriate threshold of the mean expression and dispersion. The top 2000 variable genes were used to identify anchors between different samples by utilizing the FindIntegrationAnchors function. Then, the IntegrateData function was applied to perform data integration with these anchors. An assay of integrated data from all cells was generated for downstream analysis.

Clustering and dimensionality reduction. The Seurat R package and specific functions were applied for clustering and reducing data dimensions. The integrated data were utilized to identify gene features with significant variations across all cells by employing the FindVariableFeatures function. The top 2000 highly variable genes were scaled and centered with the ScaleData function. Dimensionality reduction was then performed via the principal component analysis (PCA) with 30 principal components being processed using the RunPCA function. Graph-based unsupervised clustering was performed to optimize cluster resolution and identify cell clusters with the FindNeighbors and FindClusters functions. The visualization was realized by the RunUMAP function.

Cell type assignment. An unbiased recognition of cell types was performed by using the SingleR package (version 1.4.1). Briefly, DEGs were clustered according to gene markers of different cell types in the reference transcriptomic datasets. The assigned cell types and corresponding markers were then manually checked with marker collections from previous publications and those from the CellMarker database. DEGs in each cell type were then identified by using the FindAllMarkers function.

Cell-cell communication analysis. The R package CellChat (version 1.1.3) was used to identify the potential interactions between different cell populations. The CellChatDB murine database was imported to construct the ligand-receptor interactions. Cell-cell interaction probability values were calculated and visualized with circle plots.

Functional enrichment analysis. Functional enrichment analysis was conducted using the ClusterProfiler R package (version 4.1). Gene set enrichment analysis (GSEA) was performed using the gsea function. DEGs in each cell type or cluster were analyzed to identify enriched GO biological processes or KEGG pathways. An adjusted p value < 0.05 was considered significantly enriched.

Trajectory analysis. Pseudotime trajectory analysis was performed with Monocle2[75]. To construct the trajectory, the top 2000 highly variable genes were selected by using the FindVariableFeatures function in Seurat (version 4.0). The dimensionality reduction was performed by employing the DDRTree algorithm. And the trajectory was visualized by performing the plot_cell_trajectory function.

Analysis of PPI network. The STRING database (https://cn.string-db.org/) was used to analyze the PPI network of DEGs. The minimum required interaction score was set as 0.900. The PPI network generated was imported into the Cytoscape software for removing interactions with fewer than 4 connections.

Spatial transcriptomic analysis

The Seurat R package was used for analyzing the spatial transcriptomic data. The raw image data were converted into a digital matrix using the software Visium Spatial Gene Expression Solution and were then imported into R for further analysis. Data filtering was performed using the FilterCells and FilterGenes functions to remove low-quality cells and genes with low expression or high noise. The gene expression values were normalized with the SCtransform method provided in Seurat. The high-dimensional gene expression data were reduced to a lower dimension using PCA and t-distributed stochastic neighbor embedding (t-SNE) algorithms, via the RunPCA and RunTSNE functions, respectively. Cells were then clustered into distinct cell populations using the FindClusters function. To identify marker genes for each cell population, the FindAllMarkers function was used, which analyzes DEGs between each cluster and all other clusters. Spatial visualization of different cell populations distributed in the brain sections was performed using the SpatialDimPlot and FeaturePlot functions. The single-cell data was integrated with the FindTransferAnchors and TransferData functions.

Electron microscopy

1 mm^3 of hippocampal tissue was fixed with the electron microscopy fixation solution containing 2.5% glutaraldehyde (Servicebio) in PBS for at least 6 h and was washed with

PBS 3 times, 15 min each. Then the tissue was further fixed in 2% osmium tetroxide (OsO_4, in PBS) for 2 h, followed by 3 washes in PBS, 15 min each. The dehydration of the tissue was first performed with a series of alcohols at 4°C: 50% ethanol, 70% ethanol, 90% ethanol, 90%ethanol: 90% acetone (1:1), 90% acetone, and finally with 100% acetone at room temperature 3 times, 15-20 min each. Afterwards, the tissue was embedded at room temperature in 100% acetone: embedding solution (3:1), 100% acetone: embedding solution (3:1) overnight, and at 37°C in pure embedding solution 3 times, 2-3 h each. Sections of 50-60 nm were obtained with an ultramicrotome (Leica) and subjected to double staining of uranyl acetate and lead citrate. The images were acquired on a transmission electron microscope (Hitachi, Ltd).

Mitochondrial function-related assays

The levels of ATP, glucose, lactic acid, pyruvic acid, H_2O_2, SOD activity, CAT activity, MMP, mPTP and ROS were determined with commercially available assay kits (Beyotime, Nanjing Jiancheng Bioengineering Institute, Boxbio, and Servicebio) according to the manufacturers' instructions.

Immunofluorescence labeling

Immunohistochemistry. Adult mice at specific ages were anesthetized with 1.25% tribromoethanol (250mg/kg) and perfused transcardially with ice-cold PBS and then with 4% paraformaldehyde (PFA). The mouse brains were fixed in 4% PFA for 6 h, dehydrated in 30% sucrose (in PBS) for 48 h, and embedded in Tissue-Tek® O.C.T. compound (Sakura® Finetek). Coronal sections of 20 μm were obtained using a CM1950 cryostat (Leica) and were mounted onto adhesive slides (Citotest). Then sections were washed with PBS, permeabilized with 1×PBST (0.1% Triton X-100 in PBS), blocked with 10% goat serum (in PBS), and incubated in primary antibodies diluted in 10% goat serum (in PBS) at 4°C overnight. After the primary antibody incubation, sections were washed with PBS 3 times, followed by the incubation of secondary antibodies diluted in PBS at room temperature for 2 h. Finally, the sections were washed with PBS, stained with DAPI (10 μg/mL in PBS, Solarbio) and imaged with a confocal microscope (Zeiss). Images were analyzed with ImageJ.

Immunocytochemistry. Cells were plated on glass coverslips coated with 0.1% poly-L-lysine. The culture medium was aspirated, and cells were washed with PBS. Cells were fixed with 4% PFA for 10 min. The permeabilization, blocking, antibody staining and imaging of cells followed the same steps described above for brain sections.

Western blotting

Mouse hippocampi or cultured cells were collected and homogenized in ice-cold lysis buffer (Beyotime) containing protease inhibitor (Beyotime). The lysates were centrifuged at 15,000 rpm at 4°C for 10 min. The supernatant was removed, and the pellet was resuspended in 5×SDS-PAGE protein loading buffer (Yeasen Biotechnology) and denatured at 95°C for 5 min. The concentration of the protein was determined with a BCA protein assay kit. 25-30 μg of protein was loaded and separated in 6%-15% SDS gels prepared using the Omni-Easy™ PAGE Gel Fast Preparation Kit (Shanghai Epizyme Biomedical Technology) and were then transferred to NC transfer membranes (PALL). The membranes were blocked with 5% BSA (Servicebio) or Rapid Blocking Buffer (Servicebio) and were incubated with primary antibodies diluted in blocking buffer at 4°C overnight. After the incubation, the membranes were washed with 1×TBST (0.5% Tween-20 in tris-buffered saline) 4 times, 10 min each. The membranes were incubated with fluorescent secondary antibodies (SeraCare Life Sciences) diluted in blocking buffer at room temperature for 1h, followed by 3 washes with 1×TBST. GAPDH, Na^+-K^+ ATPase, β-tubulin or histone H3 were used as the loading control. Protein bands were visualized with an infrared scanner (Odyssey, LI-COR, USA). Intensities of protein bands were quantified with ImageJ.

Co-immunoprecipitation

Cells were lysed in lysis buffer containing protease inhibitor and were centrifuged at 14,000 rpm at 4°C for 15 min. The supernatant was collected as protein lysate. 3 μg of antibody was diluted in 200 μL of 1×PBST and was incubated with protein A/G magnetic beads (ABclonal Technology) at room temperature for 2 h, followed by the addition of around 500 μg of protein lysate in 1 mL. The mixture of the antibody, beads and proteins were incubated on a rotator at 4°C overnight and were collected with a magnetic separator. The mixture was washed three times with NT2 buffer (50 mM Tris-HCl, PH 7.4, 150 mM NaCl, 1 mM $MgCl_2$, 0.05% Nonidet P-40), resuspended in 30 μL of 2×SDS-PAGE loading buffer, and denatured at 95°C for 10 min. Western blotting was performed afterwards to determine the components of the co-immunoprecipitated protein complex.

Quantitative PCR (qPCR)

Total RNA, cytoplasmic RNA and nuclear RNA were extracted from cells and brain tissues with Trizol RNA extraction solution (Servicebio). First-strand cDNAs were synthesized with HiScript II Q Select RT SuperMix (Vazyme Biotech) and diluted 10-fold with sterile distilled water (dH_2O). Real-time qPCR was performed using 10 μL of Genious 2×SYBR Green Fast qPCR Mix (No ROX) (ABclonal), 0.4 μL of each primer (10 μM), 9.2 μL of diluted cDNA, with the following programme: 95°C for 3 min; 40 cycles of 95°C for 5 s, 60°C for 30 s; 95°C for 5 s; 60 repeats of an increment of 0.5°C from 65°C to 95°C, 5s for each repeat. Each reaction included 4 technical replicates and was repeated to generate at least 3 biological replicates. The relative mRNA level of each gene was normalized to that of *GAPDH/Gapdh*.

Electrophysiology

Electrophysiology was performed as previously described[76]. Briefly, mice were anesthetized and perfused immediately with ice-cold NMDG artificial cerebrospinal fluid (ACSF, in mM) (93 HCl, 93 NMDG, 1.25 NaH_2PO_4, 10 $MgSO_4$, 2.5 KCl, 30 $NaHCO_3$, 25 glucose, 0.5 $CaCl_2$, 20 HEPES, 5 sodium ascorbate, 3 sodium pyruvate, 2 thiourea, pH 7.4). Sagittal brain slices containing the hippocampus were cut on a vibratome (VT-1200S, Leica Microsystems), incubated in oxygenated NMDG ACSF at 32°C for 10-15 min, and were then kept in normal oxygenated ACSF (in mM: 2.5 KCl, 126 NaCl, 10 glucose, 1.25 NaH_2PO_4, 2 $MgSO_4$, 26 $NaHCO_3$, 2 $CaCl_2$) at room temperature for 1 h. Recordings were performed with an MultiClamp 700B amplifier and a Digidata 1440A digitizer (Molecular Devices). Patch electrodes (3-5 MΩ) were filled with a solution containing (in mM): 130 K-gluconate, 8 NaCl, 10 HEPES, 1 EGTA, 2 $MgCl_2$, 2 ATP, and 0.2 GTP. For the current clamp recording, a series of current steps of 400 ms from -50 pA to 200 pA in 50 pA increments were applied. In the voltage clamp recording, (-)-bicuculline methochloride (50 μM; Abcam) and tetrodotoxin citrate (1 μM; Bio-Techne) were used to record mEPSCs. Data were collected and analyzed using the pClamp10 software (Molecular Devices) and the Clampfit 10.4 software (Molecular Devices) respectively.

Microglial phagocytosis assay

To determine the Aβ phagocytic capacity of microglia *in vitro*, 1 μmol/μL $Aβ_{1-42}$ was added to the culture medium of BV2 cells and incubated with the cells for 6 h. Then the nucleus was stained with DAPI, and the images were taken with a confocal microscope. The percentage of $Aβ_{1-42}$-positive ($Aβ^+$) cells was quantified to represent the degree of Aβ phagocytosis. For the phagocytosis assay of fluorescent microshperes, BV2 cells were cultured with a density of $2x10^4$ on 1.5 mm^2 coverslips. Fluorescently labeled microspheres (Sigma-Aldrich) were added at a concentration of 1μL/mL and incubated with the cells for 6 h. Then cells were washed with PBS to remove unengulfed microspheres, fixed with 4% PFA, and stained with Actin-Tracker Red-594 (Beyotime) and DAPI for the visualization of intracellular microfilaments and nuclei respectively. The numbers of fluorescent microspheres in at least 6 cells were counted to quantify the phagocytic capacity.

Chronic inflammation induction

Different groups of mice were intraperitoneally injected with LPS (1µg/mL) or PBS. 3 h later, the mice were euthanized, and the hippocampi and cortices were collected to determine the expression levels of proinflammatory cytokines and related factors.

Determination of lysosomal integrity

BV2 cells were treated with 1 mM L-Leucyl-L-Leucine methyl ester hydrobromide (LLOMe) to induce lysosomal impairments, and then were fluorescently immunolabeled with antibodies against Galectin-3 and LC3. Different groups of cells were viewed on a confocal microscope at 0h, 2h, 4h and 8h after the addition of LLOMe. More double staining of Galectin-3 and LC3 indicates poorer lysosomal recovery.

Measurement of intracellular lipid level

BV2 cells were incubated with the BODIPY neutral lipid droplet fluorescent probe according to the manufacturer’s instructions (Maokang Biotechnology). The percentage of BODIPY-positive cells was calculated to show the intracellular lipid level.

ChIP-qPCR

1×10^7 cells were fixed with 1% formaldehyde at room temperature for 10 min. A final concentration of 125 mM glycine was added and incubated with the cells for 5 min with gentle shaking. Then cells were washed with PBS, collected, and lysed in lysis buffer. Sonification was performed followed by centrifugation at 14,000 rpm at 4°C for 10 min to collect the supernatant containing chromatin fragments. Antibodies against SOX2 or histone H3 (H3K27ac or H3k27me3) or IgG were added and incubated with the supernatant on a rotator at 4°C overnight. Subsequently, ChIP-grade protein A/G magnetic beads (ABclonal Technology) were added and incubated with the immunoprecipitated samples with shaking at 4°C for 1 h. Then the beads were collected with a magnetic separator and the immunoprecipitated complexes were released by adding 300 µL elution buffer to the beads. Reverse cross-linking was performed by adding 15 µL proteinase K (20mg/mL) and incubating at 65 °C overnight. Finally, DNAs were purified with a DNA purification kit (Wuhan Fine Biotech Co., Ltd.) and subjected to qPCR using ChIP-qPCR-specific primers.

Statistical analysis

All quantitative data are shown as mean ± s.e.m. Statistical analyses were performed in GraphPad Prism 9.3.1 and Microsoft 365 Excel. For determining the difference between two groups, unpaired two-tailed t-test was performed. For comparing the behavioral performances of different mouse groups that bore different pre-treatments, two-way ANOVA with Tukey’s (for data of Morris water maze test) or Šídák's (for data of Y maze test) multiple comparison tests was used. For comparing the survival curves of mice, the Log-rank (Mantel-Cox) test was used. To fit the regression curve of *ATP11B* expression trend with the increase of age in normal human DLPFC, a 2nd order polynomial model was generated. The PCC for evaluating gene expression correlation was generated by linear regression. The significance levels were set at *$P < 0.05$, ** $P < 0.01$, *** $P < 0.001$, and **** $P < 0.0001$.

Data availability

All data supporting the findings of this study can be found within the article. Single-cell RNA-seq data have been deposited at GEO and are publicly available as of the date of publication. All code is included in previously established R and Python packages. Any additional information required to reanalyze the data reported in this paper is available from the corresponding authors upon request.

Acknowledgments

This work was supported by the CAMS Initiative for Innovative Medicine (2022-I2M-1-012); State Key Laboratory Special Fund 2060204; the National Key R&D Program of China (2020YFA0113000); the Key-Area Research and Development Program of Guangdong Province (2021B0909060001); Supported by the 111 Project (B18007); the National Natural Science Foundation of China (82300129).

Conflict of interests

The authors declare no competing interests.

Author Contributions

S.B.Z. performed immunostaining and behavioral experiments and assisted in PET/CT scan. R.Q.S. performed mitochondrial dynamics and function-related assays and analysis. C.S.L. performed l-DNB analysis. H.W., J.X.Z., and P.R.W. analyzed RNAseq and transcriptomics data. N.J.D. performed co-immunoprecipitation. W.X.Q. performed ChIP-qPCR. H.W.S. performed electron microscopy experiments. C.P.L performed synaptic function-related evaluations. S.B.Z., R.Q.S. and W.X.Q. performed qPCR. L.H., W.W.Z. and X.T.L. performed western blotting. J.Y.Z. assisted in data collection and figure preparation. J.T.G., S.J.M., D.L. and X.Y.A. assisted in data analysis. R.C.Z., L.N.C., X.P.L., J.W. and Q.L. supervised the study. T.Q.W., Q.H., R.J.Z., S.H.W., H.L.L. and J.L. contributed to the design of the study. Q.L. wrote the manuscript. E.B. reviewed the manuscript. All the authors have approved the final version of the manuscript.

References

1. DeTure, M. A. & Dickson, D. W. The neuropathological diagnosis of Alzheimer's disease. *Mol Neurodegeneration* **14**, 32 (2019).
2. Lee, J. C., Kim, S. J., Hong, S. & Kim, Y. Diagnosis of Alzheimer's disease utilizing amyloid and tau as fluid biomarkers. *Exp Mol Med* **51**, 1–10 (2019).
3. Graff-Radford, J. *et al.* New insights into atypical Alzheimer's disease in the era of biomarkers. *The Lancet Neurology* **20**, 222–234 (2021).
4. Patel, H. *et al.* Transcriptomic analysis of probable asymptomatic and symptomatic alzheimer brains. *Brain, Behavior, and Immunity* **80**, 644–656 (2019).
5. Tzioras, M., McGeachan, R. I., Durrant, C. S. & Spires-Jones, T. L. Synaptic degeneration in Alzheimer disease. *Nat Rev Neurol* **19**, 19–38 (2023).
6. Wang, W., Zhao, F., Ma, X., Perry, G. & Zhu, X. Mitochondria dysfunction in the pathogenesis of Alzheimer's disease: recent advances. *Mol Neurodegeneration* **15**, 30 (2020).
7. Ryu, W.-I. *et al.* Brain cells derived from Alzheimer's disease patients have multiple specific innate abnormalities in energy metabolism. *Mol Psychiatry* **26**, 5702–5714 (2021).
8. Wang, X. & Zheng, W. Ca $^{2+}$ homeostasis dysregulation in Alzheimer's disease: a focus on plasma membrane and cell organelles. *FASEB j.* **33**, 6697–6712 (2019).
9. Chen, L., Liu, R., Liu, Z.-P., Li, M. & Aihara, K. Detecting early-warning signals for sudden deterioration of complex diseases by dynamical network biomarkers. *Sci Rep* **2**, 342 (2012).
10. Liu, X., Liu, R., Zhao, X.-M. & Chen, L. Detecting early-warning signals of type 1 diabetes and its leading biomolecular networks by dynamical network biomarkers. *BMC Med Genomics* **6**, S8 (2013).
11. Chen, P., Liu, R., Chen, L. & Aihara, K. Identifying critical differentiation state of MCF-7 cells for breast cancer by dynamical network biomarkers. *Front. Genet.* **6**, (2015).
12. Yang, B. *et al.* Dynamic network biomarker indicates pulmonary metastasis at the tipping point of hepatocellular carcinoma. *Nat Commun* **9**, 678 (2018).

13. Raj, T. *et al.* Integrative transcriptome analyses of the aging brain implicate altered splicing in Alzheimer's disease susceptibility. *Nat Genet* **50**, 1584–1592 (2018).

14. De Jager, P. L. *et al.* A multi-omic atlas of the human frontal cortex for aging and Alzheimer's disease research. *Sci Data* **5**, 180142 (2018).

15. Aihara, K., Liu, R., Koizumi, K., Liu, X. & Chen, L. Dynamical network biomarkers: Theory and applications. *Gene* **808**, 145997 (2022).

16. Taanman, J.-W. The mitochondrial genome: structure, transcription, translation and replication. *Biochimica et Biophysica Acta (BBA) - Bioenergetics* **1410**, 103–123 (1999).

17. Berth, S. H. & Lloyd, T. E. Disruption of axonal transport in neurodegeneration. *Journal of Clinical Investigation* **133**, e168554 (2023).

18. Dias, C. & Nylandsted, J. Plasma membrane integrity in health and disease: significance and therapeutic potential. *Cell Discov* **7**, 4 (2021).

19. Pfanner, N., Warscheid, B. & Wiedemann, N. Mitochondrial proteins: from biogenesis to functional networks. *Nat Rev Mol Cell Biol* **20**, 267–284 (2019).

20. Zhang, P., Konja, D., Zhang, Y. & Wang, Y. Communications between Mitochondria and Endoplasmic Reticulum in the Regulation of Metabolic Homeostasis. *Cells* **10**, 2195 (2021).

21. Kosicek, M. & Hecimovic, S. Phospholipids and Alzheimer's Disease: Alterations, Mechanisms and Potential Biomarkers. *IJMS* **14**, 1310–1322 (2013).

22. Wang, J. *et al.* ATP11B deficiency leads to impairment of hippocampal synaptic plasticity. *Journal of Molecular Cell Biology* **11**, 688–702 (2019).

23.Snowden, S. G. *et al.* Neurotransmitter Imbalance in the Brain and Alzheimer's Disease Pathology. *JAD* **72**, 35–43 (2019).

24. Bonora, M., Giorgi, C. & Pinton, P. Molecular mechanisms and consequences of mitochondrial permeability transition. *Nat Rev Mol Cell Biol* **23**, 266–285 (2022).

25. Yao, P. J. *et al.* Sonic hedgehog pathway activation increases mitochondrial abundance and activity in hippocampal neurons. *MBoC* **28**, 387–395 (2017).

26. Hall, A. R., Burke, N., Dongworth, R. K. & Hausenloy, D. J. Mitochondrial fusion and fission proteins: novel therapeutic targets for combating cardiovascular disease: Mitochondrial dynamics and the heart. *Br J Pharmacol* **171**, 1890–1906 (2014).

27. Choi, G. E. *et al.* Glucocorticoid-mediated ER-mitochondria contacts reduce AMPA receptor and mitochondria trafficking into cell terminus via microtubule destabilization. *Cell Death Dis* **9**, 1137 (2018).

28. Ziebell, J. M., Adelson, P. D. & Lifshitz, J. Microglia: dismantling and rebuilding circuits after acute neurological injury. *Metab Brain Dis* **30**, 393–400 (2015).

29. Ladeby, R. *et al.* Microglial cell population dynamics in the injured adult central nervous system. *Brain Research Reviews* **48**, 196–206 (2005).

30. Qin, L. *et al.* Systemic LPS causes chronic neuroinflammation and progressive neurodegeneration. *Glia* **55**, 453–462 (2007).

31. Jurga, A. M., Paleczna, M. & Kuter, K. Z. Overview of General and Discriminating Markers of Differential Microglia Phenotypes. *Front. Cell. Neurosci.* **14**, 198 (2020).

32. Simpson, D. S. A. & Oliver, P. L. ROS Generation in Microglia: Understanding Oxidative Stress and Inflammation in Neurodegenerative Disease. *Antioxidants* **9**, 743 (2020).

33. Wang, L. *et al.* Glucose transporter 1 critically controls microglial activation through facilitating glycolysis. *Mol Neurodegeneration* **14**, 2 (2019).

34. Lauro, C. & Limatola, C. Metabolic Reprograming of Microglia in the Regulation of the Innate Inflammatory Response. *Front. Immunol.* **11**, 493 (2020).

35. Voloboueva, L. A., Emery, J. F., Sun, X. & Giffard, R. G. Inflammatory response of microglial BV-2 cells includes a glycolytic shift and is modulated by mitochondrial glucose-regulated protein 75/mortalin. *FEBS Letters* **587**, 756–762 (2013).

36. Gimeno-Bayón, J., López-López, A., Rodríguez, M. J. & Mahy, N. Glucose pathways adaptation supports acquisition of activated microglia phenotype: Activated Microglia Metabolic Reprogramming. *Journal of Neuroscience Research* **92**, 723–731 (2014).

37. Nair, S. *et al.* Lipopolysaccharide-induced alteration of mitochondrial morphology induces a metabolic shift in microglia modulating the inflammatory response in vitro and in vivo. *Glia* **67**, 1047–1061 (2019).

38. Marschallinger, J. *et al.* Lipid-droplet-accumulating microglia represent a dysfunctional and proinflammatory state in the aging brain. *Nat Neurosci* **23**, 194–208 (2020).

39. Loving, B. A. & Bruce, K. D. Lipid and Lipoprotein Metabolism in Microglia. *Front. Physiol.* **11**, 393 (2020).

40. Amador-Arjona, A. *et al.* SOX2 primes the epigenetic landscape in neural precursors enabling proper gene activation during hippocampal neurogenesis. *Proc. Natl. Acad. Sci. U.S.A.* **112**, (2015).

41. Kuwabara, T. *et al.* Wnt-mediated activation of NeuroD1 and retro-elements during adult neurogenesis. *Nat Neurosci* **12**, 1097–1105 (2009).

42. Agathocleous, M. *et al.* A directional Wnt/β-catenin-Sox2-proneural pathway regulates the transition from proliferation to differentiation in the *Xenopus* retina. *Development* **136**, 3289–3299 (2009).

43. Baltus, G. A. *et al.* Acetylation of Sox2 Induces its Nuclear Export in Embryonic Stem Cells. *Stem Cells* **27**, 2175–2184 (2009).

44. Liao, W. *et al.* Dual Specificity Phosphatase 6 Protects Neural Stem Cells from β-Amyloid-Induced Cytotoxicity through ERK1/2 Inactivation. *Biomolecules* **8**, 181 (2018).

45. Li, M. *et al.* Differentially Expressed Genes in the Brain of Aging Mice With Cognitive Alteration and Depression- and Anxiety-Like Behaviors. *Front. Cell Dev. Biol.* **8**, 814 (2020).

46. Mufson, E. J. *et al.* Mild cognitive impairment: pathology and mechanisms. *Acta Neuropathol* **123**, 13–30 (2012).

47. Mota, S. I. *et al.* Oxidative stress involving changes in Nrf2 and ER stress in early stages of Alzheimer’s disease. *Biochimica et Biophysica Acta (BBA) - Molecular Basis of Disease* **1852**, 1428–1441 (2015).

48. Valla, J. *et al.* Reduced Posterior Cingulate Mitochondrial Activity in Expired Young Adult Carriers of the APOE ε4 Allele, the Major Late-Onset Alzheimer's Susceptibility Gene. *JAD* **22**, 307–313 (2010).

49. Du, H. *et al.* Early deficits in synaptic mitochondria in an Alzheimer's disease mouse model. *Proc. Natl. Acad. Sci. U.S.A.* **107**, 18670–18675 (2010).

50. Yao, J. *et al.* Mitochondrial bioenergetic deficit precedes Alzheimer's pathology in female mouse model of Alzheimer's disease. *Proc. Natl. Acad. Sci. U.S.A.* **106**, 14670–14675 (2009).

51. Klein, H.-U. *et al.* Characterization of mitochondrial DNA quantity and quality in the human aged and Alzheimer's disease brain. *Mol Neurodegeneration* **16**, 75 (2021).

52. Kadenbach, B. & Hüttemann, M. The subunit composition and function of mammalian cytochrome c oxidase. *Mitochondrion* **24**, 64–76 (2015).

53. Bi, R. *et al.* Genetic association of the cytochrome c oxidase-related genes with Alzheimer's disease in Han Chinese. *Neuropsychopharmacol* **43**, 2264–2276 (2018).

54. Drzezga, A. *et al.* Prediction of individual clinical outcome in MCI by means of genetic assessment and (18)F-FDG PET. *J Nucl Med* **46**, 1625–1632 (2005).

55. Dong, Q.-Y. *et al.* Glucose metabolism in the right middle temporal gyrus could be a potential biomarker for subjective cognitive decline: a study of a Han population. *Alz Res Therapy* **13**, 74 (2021).

56. Strom, A. *et al.* Cortical hypometabolism reflects local atrophy and tau pathology in symptomatic Alzheimer's disease. *Brain* **145**, 713–728 (2022).

57. Rangaraju, V., Calloway, N. & Ryan, T. A. Activity-Driven Local ATP Synthesis Is Required for Synaptic Function. *Cell* **156**, 825–835 (2014).

58. Ashrafi, G., De Juan-Sanz, J., Farrell, R. J. & Ryan, T. A. Molecular Tuning of the Axonal Mitochondrial Ca2+ Uniporter Ensures Metabolic Flexibility of Neurotransmission. *Neuron* **105**, 678-687.e5 (2020).

59. Li, S. & Sheng, Z.-H. Energy matters: presynaptic metabolism and the maintenance of synaptic transmission. *Nat Rev Neurosci* **23**, 4–22 (2022).

60. Henley, J. M. & Wilkinson, K. A. Synaptic AMPA receptor composition in development, plasticity and disease. *Nature Reviews Neuroscience* **17**, 337–350 (2016).

61. Kaushal, J. B., Popli, P., Sankhwar, P., Shukla, V. & Dwivedi, A. Sonic hedgehog protects endometrial hyperplasial cells against oxidative stress via suppressing mitochondrial fission protein dynamin-like GTPase (Drp1). *Free Radical Biology and Medicine* **129**, 582–599 (2018).

62. Fairley, L. H., Wong, J. H. & Barron, A. M. Mitochondrial Regulation of Microglial Immunometabolism in Alzheimer's Disease. *Front. Immunol.* **12**, 624538 (2021).

63. Joshi, A. U. *et al.* Fragmented mitochondria released from microglia trigger A1 astrocytic response and propagate inflammatory neurodegeneration. *Nat Neurosci* **22**, 1635–1648 (2019).

64. Andersson, A. K., Rönnbäck, L. & Hansson, E. Lactate induces tumour necrosis factor-α, interleukin-6 and interleukin-1β release in microglial- and astroglial-enriched primary cultures: Lactate induces glial cell cytokine release. *Journal of Neurochemistry* **93**, 1327–1333 (2005).

65. Hu, C. *et al.* Energy Metabolism Plays a Critical Role in Stem Cell Maintenance and Differentiation. *IJMS* **17**, 253 (2016).

66. Rehman, J. Empowering self-renewal and differentiation: the role of mitochondria in stem cells. *J Mol Med* **88**, 981–986 (2010).

67. Wang, W. *et al.* Mitochondrial DNA Integrity Is Essential For Mitochondrial Maturation During Differentiation of Neural Stem Cells. *Stem Cells* **28**, 2195–2204 (2010).

68. Lee, H.-R. *et al.* Discovery of a Small Molecule that Enhances Astrocytogenesis by Activation of STAT3, SMAD1/5/8, and ERK1/2 via Induction of Cytokines in Neural Stem Cells. *ACS Chem. Neurosci.* **7**, 90–99 (2016).

69. Semprich, C. I. *et al.* ERK1/2 signalling dynamics promote neural differentiation by regulating chromatin accessibility and the polycomb repressive complex. *PLoS Biol* **20**, e3000221 (2022).

70. Lee, J.-A., Jang, D.-J. & Kaang, B.-K. Two major gate-keepers in the self-renewal of neural stem cells: Erk1/2 and PLCγ1 in FGFR signaling. *Mol Brain* **2**, 15, 1756-6606-2–15 (2009).

71. Tian, L. *et al.* A novel Sprouty4-ERK1/2-Wnt/β-catenin regulatory loop in marrow stromal progenitor cells controls osteogenic and adipogenic differentiation. *Metabolism* **105**, 154189 (2020).

72. Zhang, H. *et al.* Single-nucleus transcriptomic landscape of primate hippocampal aging. *Protein & Cell* **12**, 695–716 (2021).

73. Kumar, L. & Futschik, M. E. Mfuzz: A software package for soft clustering of microarray data. *Bioinformation* **2**, 5–7 (2007).

74. Wang, J. *et al.* MiR-4763-3p targeting *RASD2* as a Potential Biomarker and Therapeutic Target for Schizophrenia. *Aging and disease* **13**, 1278 (2022).

75. Qiu, X. *et al.* Reversed graph embedding resolves complex single-cell trajectories. *Nat Methods* **14**, 979–982 (2017).

76. Su, X.-Y. *et al.* Central Processing of Itch in the Midbrain Reward Center. *Neuron* **102**, 858-872.e5 (2019).

Figure legends

Fig. 1 Alterations in mitochondrial proteins and ATP11B expression mark the pre-disease state of AD. a Heatmap and landscape graph of z-transformed DNB scores for the top 20 dominant genes in an RNAseq dataset of AD. The red star marks the time point at which the average DNB score reaches its peak. **b** Circular plot of enrichment analysis for mitochondrial protein encoding genes within the dominant gene group. Ribbons indicate enriched pathways. The left outer semi-circle represents z-transformed DNB scores at stage II. The right middle semi-circle shows enrichment *P* values. **c** The PPI network of ATP11B and its related genes exhibits dynamic changes before and after AD develops. The red and blue colors represent upregulation and downregulation respectively. **d** *ATP11B* expression in normal human DLPFC. RNA levels are shown as z-scores of raw transcriptomic data. The regression line is shown as $y = -0.0009x^2 + 0.026x - 0.0007$. The chart was adapted from https://maayanlab.cloud/DLPFC. **e** A representative confocal microscopy image showing the colocalization of ATP11B and Aβ in the hippocampus of an AD patient. Scale bar: 20 μm. **f** Representative confocal microscopy images showing the colocalization of ATP11B and Aβ or IBA1 in the hippocampus of acute AD mice. The white arrowheads indicate ATP11B-expressing cells. Scale bar: 200 μm and 20 μm.

Fig.2 ATP11B deficiency induces shorter lifespan, cognitive defects, aggravation of AD pathology and mitochondrial instability. a Survival curves of wild-type and *Atp11b*$^{-/-}$ mice. **b, c** The effect of *Atp11b* knockout on the performance of young (3 months, 3M) and middle-aged (12 months, 12M) mice in Morris water maze (**b**) and Y maze (**c**) tests. **d** Representative PET/CT scan images showing the effect of *Atp11b* knockout on Aβ ([^{18}F]-AV45) and tau ([^{18}F]-PBB3) deposition in mouse brain. **e, f** The effect of *Atp11b* knockout on the performance of acute AD mice in Morris water maze (**e**) and Y maze (**f**) tests. **g** (Left) Representative electron microscopy images of mitochondria in the hippocampus of wild-type and *Atp11b*$^{-/-}$ mice. (Right) Quantification of cells containing paired or clustered mitochondria. The frequency represents the number of cells containing mitochondria in pairs or clusters. Scale bar: 500nm and 250 nm. **h** Representative western blots of MFN1, MFN2, OPA1, DRP1, FIS1, Parkin, PINK1 and OPTN, and quantification of their protein levels in the hippocampus of wild-type and *Atp11b*$^{-/-}$ mice. **i-k** Quantification of ATP levels (**i**), lactic acid levels (**j**) and ratios of lactic acid to pyruvic acid (**k**) in the hippocampus of wild-type and *Atp11b*$^{-/-}$ mice. Data in bar charts are represented as mean ± s.e.m. Log-rank (Mantel-Cox) test (**a**), $n \geq 16$ mice. Unpaired two-tailed t-test, (**b**, **c**) $n \geq 5$ mice, (**g**) $n=7$ photos, (**h-k**) $n=3$

mice. Two-way ANOVA, Tukey’s (**e**) or Šídák's (**f**) multiple comparison test, *n*≥6 mice. **P*<0.05, ***P*<0.01, ****P*<0.001, *****P*<0.0001. ns, not significant; WT, wild-type.

Fig. 3 ATP11B deficiency alters cellular distribution and intercellular communication in mouse hippocampus. a UMAP plots of single-cell RNAseq data showing cell clusters in the hippocampus of wild-type (left) and *Atp11b*$^{-/-}$ (right) mice. **b** Bar plot of the proportion of each cell cluster identified in (**a**). **c** Interaction network between different cell clusters in (**a**). The nodes represent cell types with the node size showing the interaction number. The lines represent intercellular interactions with the line thickness and transparency showing the interaction strength. **d** Quantification of the interaction number and strength shown in (**c**). **e** Interaction network between aNSCs and other types of cells in (**a**). **f** Pseudotime trajectory plot of aNSCs in (**a**). The increasingly lighter color of blue indicates the differentiation status from earlier to later stages. **g** Lineage trajectory plots showing changes in aNSCs differentiation in mouse hippocampus upon *Atp11b* knockout. **h** GO enrichment analysis of DEGs between the hippocampi of *Atp11b*$^{-/-}$ and wild-type mice. The red rectangles highlight the most significant pathways that DEGs are involved in. **i** The core module of the PPI network of DEGs between the hippocampi of *Atp11b*$^{-/-}$ and wild-type mice. The interaction number was set as ≥4. The thickness of the lines connecting interacting proteins corresponds to the interaction score. WT, wild-type.

Fig. 4 ATP11B deficiency leads to the dysregulation of memory-associated genes. a The spatial visualization of different cell populations in the coronal brain sections of *Atp11b*$^{-/-}$ and wild-type mice. The plots of spatial coordinates in the lower panel depict the position of cell clusters in the UMAP plot of the upper panel with matching colors. **b** Heatmap showing representative DEGs in the hippocampus (clusters 20 and 25) upon *Atp11b* knockout. **c** GO enrichment analysis of DEGs in the hippocampus. **d-f** Spatial plots showing the upregulation (red) or downregulation (blue) of DEGs in neurons (**d**), microglia (**e**) and aNSCs (**f**). The red squares indicate regions of difference in the regulation of DEGs between the hippocampi of *Atp11b*$^{-/-}$ and wild-type mice. WT, wild-type.

Fig. 5 ATP11B maintains mitochondrial integrity and synaptic transmission in neuronal cells. a, b Quantification of SOD and CAT activities, H_2O_2 levels, ATP levels, glucose levels, ratios of lactic acid to pyruvic acid (**a**) and mRNA levels of *MFN1*, *MFN2*, *DRP1* and *FIS1* (**b**) in *ATP11B*-silenced SH-SY5Y and control cells. **c** Representative confocal microscopy images of mitochondria in *ATP11B*-silenced SH-SY5Y and control cells. Scale bar: 10 μm. **d** Representative confocal microscopy images and quantification of MMP levels in *ATP11B*-silenced SH-SY5Y and control cells. The fluorescence intensity ratio of red JC-1 aggregates to green JC-1 monomers indicates the MMP level. Scale bar: 100 μm. **e** Representative confocal microscopy images and quantification of mPTP opening levels in *ATP11B*-silenced SH-SY5Y and control cells. The extent of mPTP opening is indicated by the loss of calcein fluorescence. Ionomycin was the positive control. Scale bar: 200 μm. **f** Representative confocal microscopy images of Parkin and LC3 in *ATP11B*-silenced SH-SY5Y and control cells. Scale bar: 10 μm. **g** Quantification of mRNA levels of *PRKN*, *PINK1*, *LC3*, *OPTN* and *p62* in *ATP11B*-silenced SH-SY5Y and control cells. **h** Representative western blots of SHH, PTCH1, SMO, GLI1, total DRP1 and p-DRP1 (serine 637), and quantification of their protein levels in *ATP11B*-silenced SH-SY5Y and control cells. **i** Representative western blots showing the effect of purmorphamine on DRP1 levels in SH-SY5Y cells with or without *ATP11B* silencing. **j** Representative western blots showing the co-immunoprecipitation of DRP1 and GLI1 in *ATP11B*-silenced SH-SY5Y and control cells. **k** Representative electron microscopy images and quantification of PSD thickness, synaptic interface curvature and synaptic cleft width in hippocampal neurons of *Atp11b*$^{-/-}$ and wild-type mice. **l** Representative recording curves and quantification of action potentials (left) and mEPSCs (right) in CA1 neurons of *Atp11b*$^{-/-}$ and wild-type mice. Data in bar and line charts are represented as mean ± s.e.m. Unpaired two-tailed t-test, (**a, b, g, h**) $n \geq 3$ batches of cells, (**d**) $n \geq 3$ regions of interest (ROIs), (**e**) $n=6$ ROIs, (**k**) $n=7$ cells, (**l**) $n=9$ cells. *$P<0.05$, **$P<0.01$, ***$P<0.001$, ****$P<0.0001$. NC, negative control; WT, wild-type; Mito, MitoTracker; IP, immunoprecipitation; p-DRP1, phosphorylated DRP1; PSD: postsynaptic density.

Fig. 6 ATP11B deficiency induces over-inflammation and impairs microglial phagocytosis. a GO enrichment analysis of DEGs in hippocampal microglia between *Atp11b*$^{-/-}$ and wild-type mice. The red square highlights a microglia-mediated pathway. **b** Representative confocal microscopy images and quantification of microglial branches in the hippocampus of *Atp11b*$^{-/-}$ and wild-type mice. Scale bar: 20 μm. **c** Representative western blots of IL1β and IL6, and quantification of their protein levels in *Atp11b*-silenced BV2 and control cells. **d** Representative confocal microscopy images and quantification of ROS levels in *Atp11b*-silenced BV2 and control cells. The ROS level is represented by the fluorescence intensity of 2',7'-dichlorofluorescein (DCF). **e** Quantification of SOD activities and ATP levels in *Atp11b*-silenced BV2 and control cells. **f, g** Representative confocal microscopy images and quantification of MMP levels (**f**) and mPTP opening levels (**g**) in *Atp11b*-silenced BV2 and control cells. The fluorescence intensity ratio of red JC-1 aggregates to green JC-1 monomers represents the MMP level. The extent of mPTP opening is indicated by the loss of calcein fluorescence, with Ionomycin being the positive control. Scale bar: 200 μm. **h**

Representative confocal microscopy images of mitochondria in *Atp11b*-silenced BV2 and control cells. Scale bar: 20 μm and 100 μm. **i** Representative confocal microscopy images and quantification of microglial phagocytosis for Aβ (left) and fluorescent microspheres (right) in *Atp11b*-silenced BV2 and control cells. The white arrows indicate Aβ-phagocytizing cells. Scale bar: 50 μm and 25 μm. Data in bar charts are represented as mean ± s.e.m. Unpaired two-tailed t-test, (**b**) *n*=9 cells from 3 mice, (**c, e**) *n*=3 batches of cells, (**d**, **f**, **g**) *n*≥5 ROIs, (**i**) *n*≥5 ROIs (left) or *n*≥6 cells (right). **P*<0.05, ***P*<0.01, ****P*<0.001, *****P*<0.0001. NC, negative control; WT, wild-type; Mito, MitoTracker; No.,number.

Fig.7 ATP11B is involved in the neuronal lineage commitment of NSCs. a GO enrichment analysis of DEGs in hippocampal aNSCs between *Atp11b*$^{-/-}$ and wild-type mice. The red squares highlight pathways related to aNSCs differentiation. **b** Correlation analysis of mRNA levels of *Atp11b* and *Sox2* in C17.2 cells. *n*=8 batches of cells. The regression line was fitted with a linear model (Y=0.0323x+2.34e-5). **c, d** Quantification of mRNA levels and cellular distribution of *Sox2* (**c**) and *β-catenin* (**d**) in *Atp11b*-silenced C17.2 and control cells. The right graph in (**d**) is a representative western blot showing the protein levels of nuclear and cytoplasmic β-catenin in *Atp11b*-silenced C17.2 and control cells. **e** Representative western blots of DUSP6, total ERK1/2, p-ERK1/2 and β-catenin, and quantification of their protein levels in *Atp11b*-silenced C17.2 and control cells. **f-h** Quantification of ATP levels (**f**), ratios of lactic acid to pyruvic acid (**g**), and mRNA levels of *Mfn1*, *Mfn2*, *Drp1* and *Fis1* (**h**) in *Atp11b*-silenced C17.2 and control cells. **i** Representative confocal microscopy images of mitochondria in *Atp11b*-silenced C17.2 and control cells. Scale bar: 20 μm. **j** Representative confocal microscopy images and quantification of mPTP opening levels in *Atp11b*-silenced C17.2 and control cells. The extent of mPTP opening is indicated by the loss of calcein fluorescence, with Ionomycin being the positive control. Scale bar: 200 μm. **k** Association of SOX2, H3K27ac and H3K27me3 with the promoter region of *Atp11b* in *Sox2*-silenced C17.2 and control cells analyzed by ChIP-qPCR. H3K27ac and H3K27me3 represent activating and repressive histone modifications respectively. Data in bar and line charts are represented as mean ± s.e.m. Unpaired two-tailed t-test, (**c-h, k**) *n*≥3 batches of cells, (**j**) *n*=6 ROIs. **P*<0.05, ***P*<0.01, ****P*<0.001, *****P*<0.0001. ns, not significant; NC, negative control; p-ERK (1/2): phosphorylated ERK1/2; Mito, MitoTracker.

Fig.8 ATP11B overexpression improves cognitive functions. a, b The effect of ATP11B overexpression on the performances of young (6 months, 6M) and middle-aged (12 months, 12M) mice in Morris water maze (**a**) and Y maze (**b**) tests. **c** The effect of ATP11B overexpression on the performances of young (5 months, 5M) and middle-aged (12 months, 12M) 3xTg-AD mice in Morris water maze. **d, e** The effect of ATP11B overexpression on the performances of young (5 months, 5M) 3xTg-AD mice in Y maze (**d**) and open field (**e**) tests. Data in bar and line charts are represented as mean ± s.e.m. Unpaired two-tailed t-test, (**a-e**) $n \geq 3$ mice, **P*<0.05, ***P*<0.01. ns, not significant; WT, wild-type; 3XTg: 3XTg AD mice; 3XTg-*ATP11B*: 3XTg AD mice with ATP11B overexpression; NO.: number.

Fig.9 Schematic summary showing the mechanism of ATP11B implicated in the activities of major brain cells via the maintenance of mitochondrial function. In neurons, ATP11B plays a critical role in maintaining an alternative SHH signaling pathway, which operates by restraining the recruitment of DRP1 to mitochondria involving direct interaction of GLI1. This impedes the phosphorylation of DRP1 at serine 637, thereby preventing excessive mitochondrial fission. The maintenance of mitochondrial dynamics sustains the regular MMP, prevents the abnormal opening of mPTP, retains SOD activity and thus inhibits the excessive release of ROS, and halts the aberrant initiation of mitophagy. In microglia, ATP11B negatively regulates the transition to the M1 pro-inflammatory phenotype, which is fueled by anaerobic glycolysis instead of oxidative phosphorylation. This metabolic switch is facilitated by increased glucose intake and is preferred under conditions of over-inflammation, typically characterized by the activation of NF-κB pathway and the production of IL1β, TNF-α and IL6. In neural stem cells, ATP11B mediates the nuclear translocation of SOX2 by ensuring adequate mitochondrial respiration and sufficient energy supply. This function is associated with the inhibition of ERK1/2 signaling pathway, which controls the initiation of neurogenesis. As a transcriptional target of SOX2, ATP11B functions as a proneural gene, actively maintaining the normal progression of neurogenesis by safeguarding mitochondrial energy production and supporting SOX2 nuclear translocation. This schematic depicts the incurred abnormal mitochondrial activities in major brain cells lacking ATP11B.

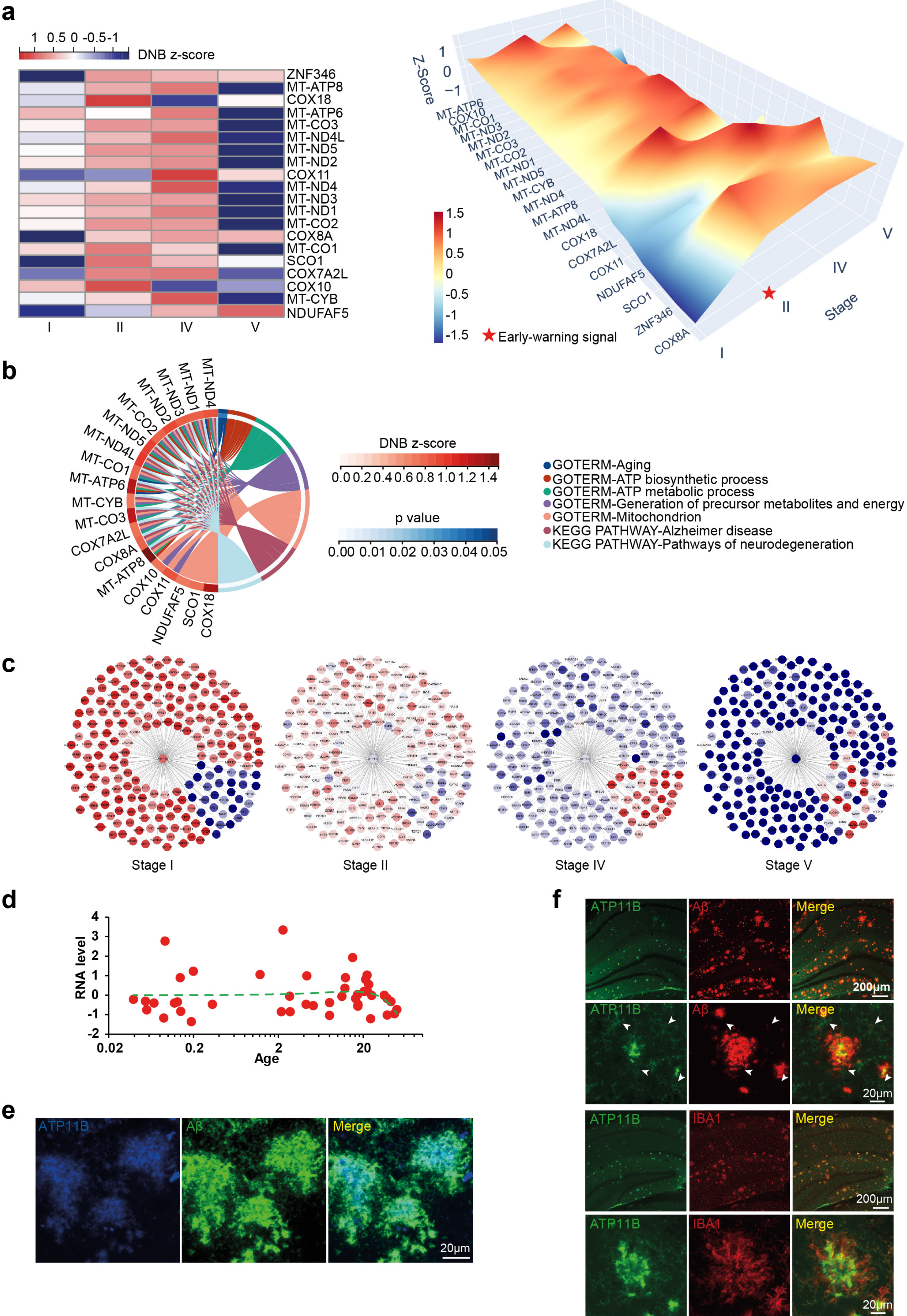
a
1 0.5 0 -0.5 -1
DNB z-score
ZNF346
MT-ATP8
COX18
MT-ATP6
MT-CO3
MT-ND4L
MT-ND5
MT-ND2
COX11
MT-ND4
MT-ND3
MT-ND1
MT-CO2
COX8A
MT-CO1
SCO1
COX7A2L
COX10
MT-CYB
NDUFAF5
I
II
IV
V
Z-Score
1
0
-1
MT-ATP6
COX10
MT-CO1
MT-ND3
MT-ND2
MT-CO3
MT-CO2
MT-ND1
MT-ND5
MT-CYB
MT-ND4
MT-ATP8
MT-ND4L
COX18
COX7A2L
COX11
NDUFAF5
SCO1
ZNF346
COX8A
1.5
1
0.5
0
-0.5
-1
-1.5
★ Early-warning signal
I
II
IV
V
Stage
b
MT-ND4
MT-ND1
MT-ND3
MT-ND2
MT-CO2
MT-ND5
MT-ND4L
MT-CO1
MT-ATP6
MT-CYB
MT-CO3
COX7A2L
COX8A
MT-ATP8
COX10
COX11
NDUFAF5
SCO1
COX18
DNB z-score
0.0 0.2 0.4 0.6 0.8 1.0 1.2 1.4
p value
0.00 0.01 0.02 0.03 0.04 0.05
● GOTERM-Aging
● GOTERM-ATP biosynthetic process
● GOTERM-ATP metabolic process
● GOTERM-Generation of precursor metabolites and energy
● GOTERM-Mitochondrion
● KEGG PATHWAY-Alzheimer disease
● KEGG PATHWAY-Pathways of neurodegeneration
c
Stage I
Stage II
Stage IV
Stage V
d
RNA level
4
3
2
1
0
-1
-2
0.02
0.2
2
20
Age
e
ATP11B
Aβ
Merge
20μm
f
ATP11B
Aβ
Merge
200μm
ATP11B
Aβ
Merge
20μm
ATP11B
IBA1
Merge
200μm
ATP11B
IBA1
Merge
20μm

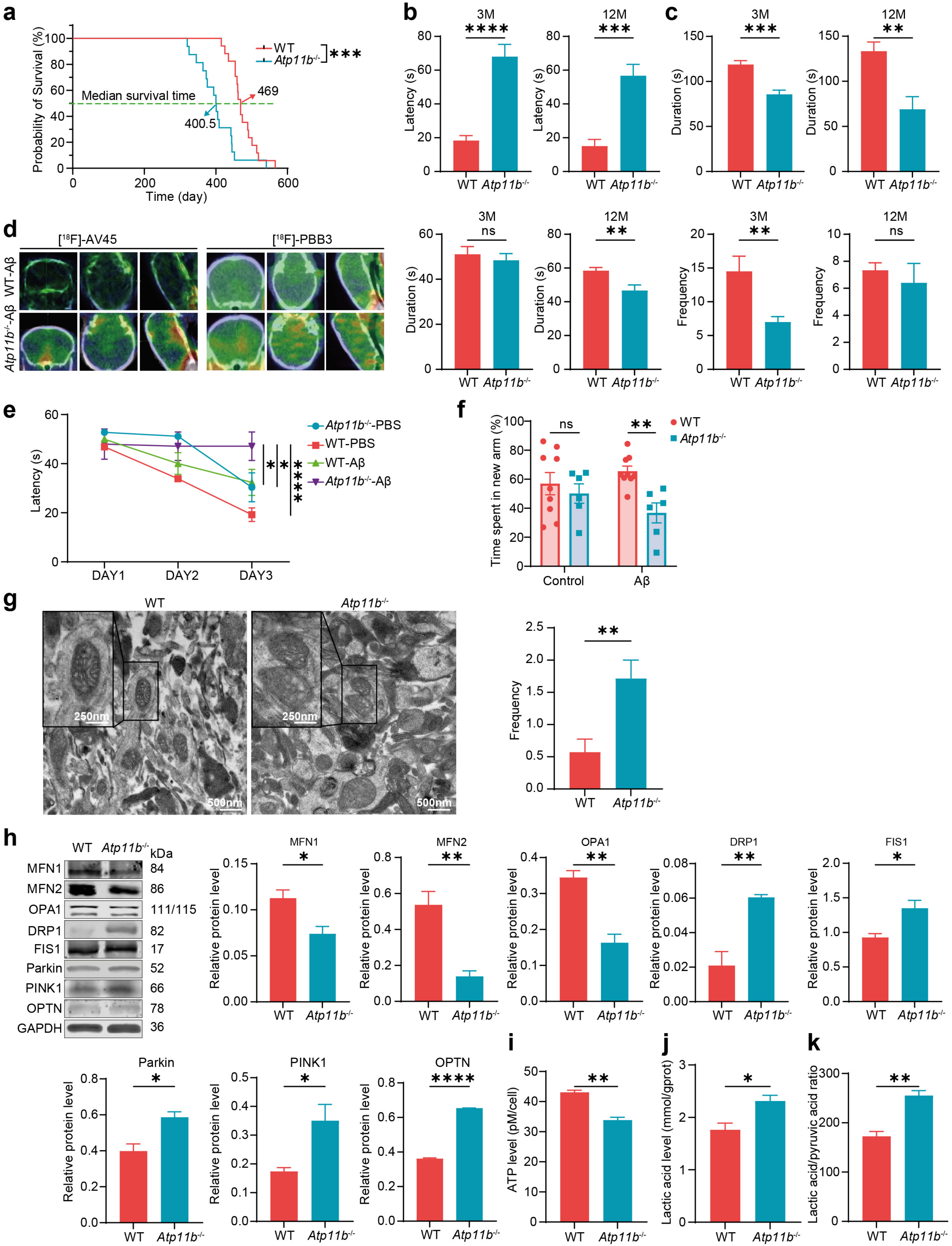
a
Probability of Survival (%)
100
80
60
40
20
0
0
200
400
600
Time (day)
WT
Atp11b-/-
***
Median survival time
469
400.5
b
3M
****
Latency (s)
WT Atp11b-/-
12M
***
c
3M
***
Duration (s)
12M
**
d
[18F]-AV45
[18F]-PBB3
WT-Aβ
Atp11b-/--Aβ
3M
ns
Duration (s)
12M
**
3M
**
Frequency
12M
ns
Frequency
e
Latency (s)
DAY1
DAY2
DAY3
Atp11b-/--PBS
WT-PBS
WT-Aβ
Atp11b-/--Aβ
*
*
****
f
Time spent in new arm (%)
Control
Aβ
ns
**
WT
Atp11b-/-
g
WT
Atp11b-/-
250nm
500nm
**
Frequency
h
WT Atp11b-/- kDa
MFN1 84
MFN2 86
OPA1 111/115
DRP1 82
FIS1 17
Parkin 52
PINK1 66
OPTN 78
GAPDH 36
MFN1 *
MFN2 **
OPA1 **
DRP1 **
FIS1 *
Relative protein level
Parkin *
PINK1 *
OPTN ****
i
ATP level (pM/cell)
**
j
Lactic acid level (mmol/gprot)
*
k
Lactic acid/pyruvic acid ratio
**

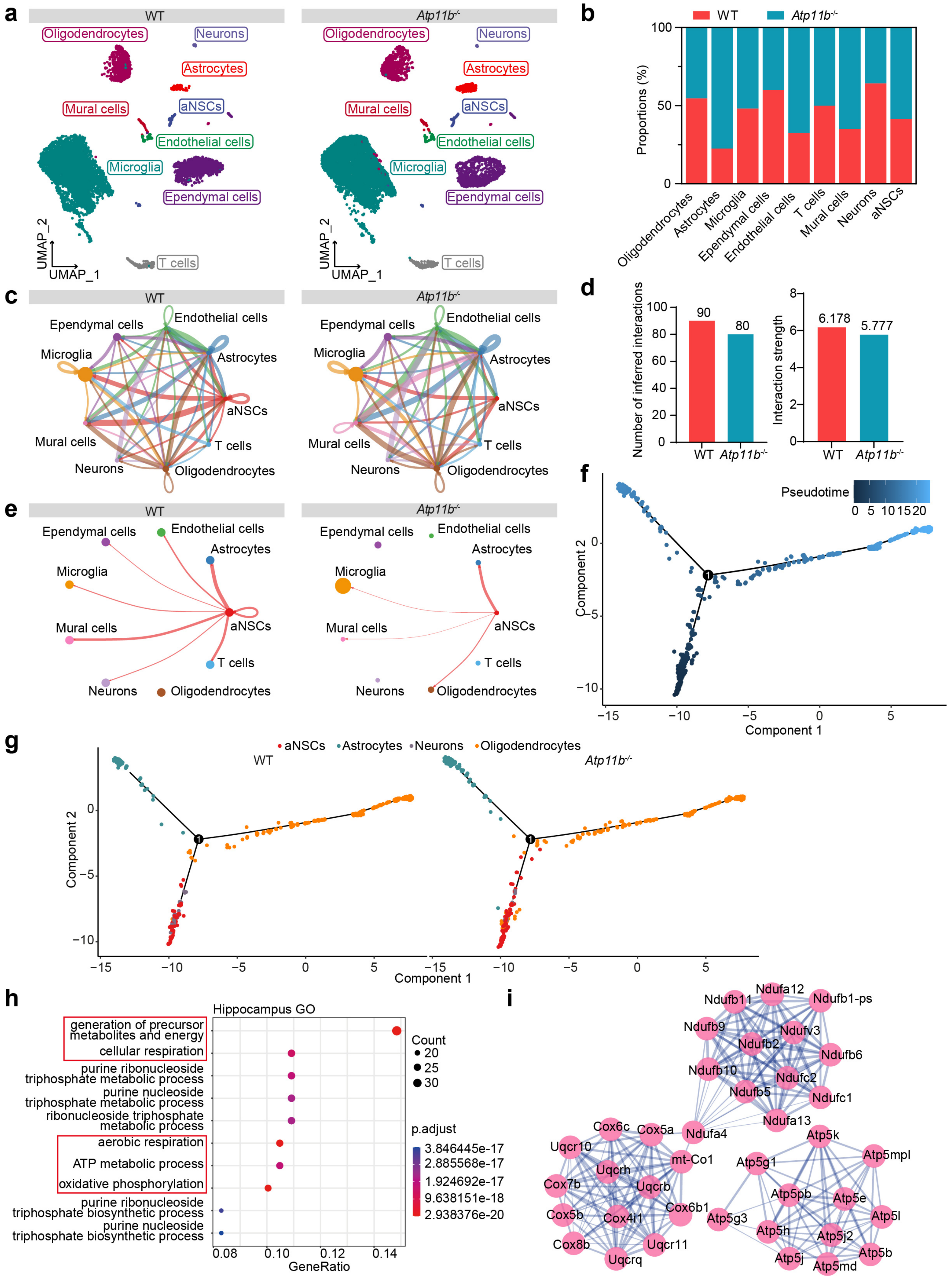
a
WT
Atp11b-/-
Oligodendrocytes
Neurons
Astrocytes
Mural cells
aNSCs
Endothelial cells
Microglia
Ependymal cells
T cells
UMAP_2
UMAP_1
b
WT
Atp11b-/-
Proportions (%)
100
50
0
Oligodendrocytes
Astrocytes
Microglia
Ependymal cells
Endothelial cells
T cells
Mural cells
Neurons
aNSCs
c
WT
Atp11b-/-
Ependymal cells
Endothelial cells
Microglia
Astrocytes
aNSCs
Mural cells
T cells
Neurons
Oligodendrocytes
d
Number of inferred interactions
90
80
Interaction strength
6.178
5.777
WT
Atp11b-/-
e
WT
Atp11b-/-
Ependymal cells
Endothelial cells
Astrocytes
Microglia
Mural cells
aNSCs
T cells
Neurons
Oligodendrocytes
f
Pseudotime
0 5 10 15 20
Component 2
Component 1
1
g
aNSCs
Astrocytes
Neurons
Oligodendrocytes
WT
Atp11b-/-
Component 2
Component 1
h
Hippocampus GO
generation of precursor metabolites and energy
cellular respiration
purine ribonucleoside triphosphate metabolic process
purine nucleoside triphosphate metabolic process
ribonucleoside triphosphate metabolic process
aerobic respiration
ATP metabolic process
oxidative phosphorylation
purine ribonucleoside triphosphate biosynthetic process
purine nucleoside triphosphate biosynthetic process
Count
20
25
30
p.adjust
3.846445e-17
2.885568e-17
1.924692e-17
9.638151e-18
2.938376e-20
0.08
0.10
0.12
0.14
GeneRatio
i
Ndufb11
Ndufa12
Ndufb1-ps
Ndufb9
Ndufv3
Ndufb2
Ndufb6
Ndufb10
Ndufc2
Ndufb5
Ndufc1
Ndufa13
Ndufa4
Cox6c
Cox5a
Uqcr10
mt-Co1
Uqcrh
Uqcrb
Cox7b
Cox6b1
Cox5b
Cox4i1
Cox8b
Uqcr11
Uqcrq
Atp5k
Atp5mpl
Atp5g1
Atp5pb
Atp5e
Atp5g3
Atp5l
Atp5h
Atp5j2
Atp5j
Atp5b
Atp5md

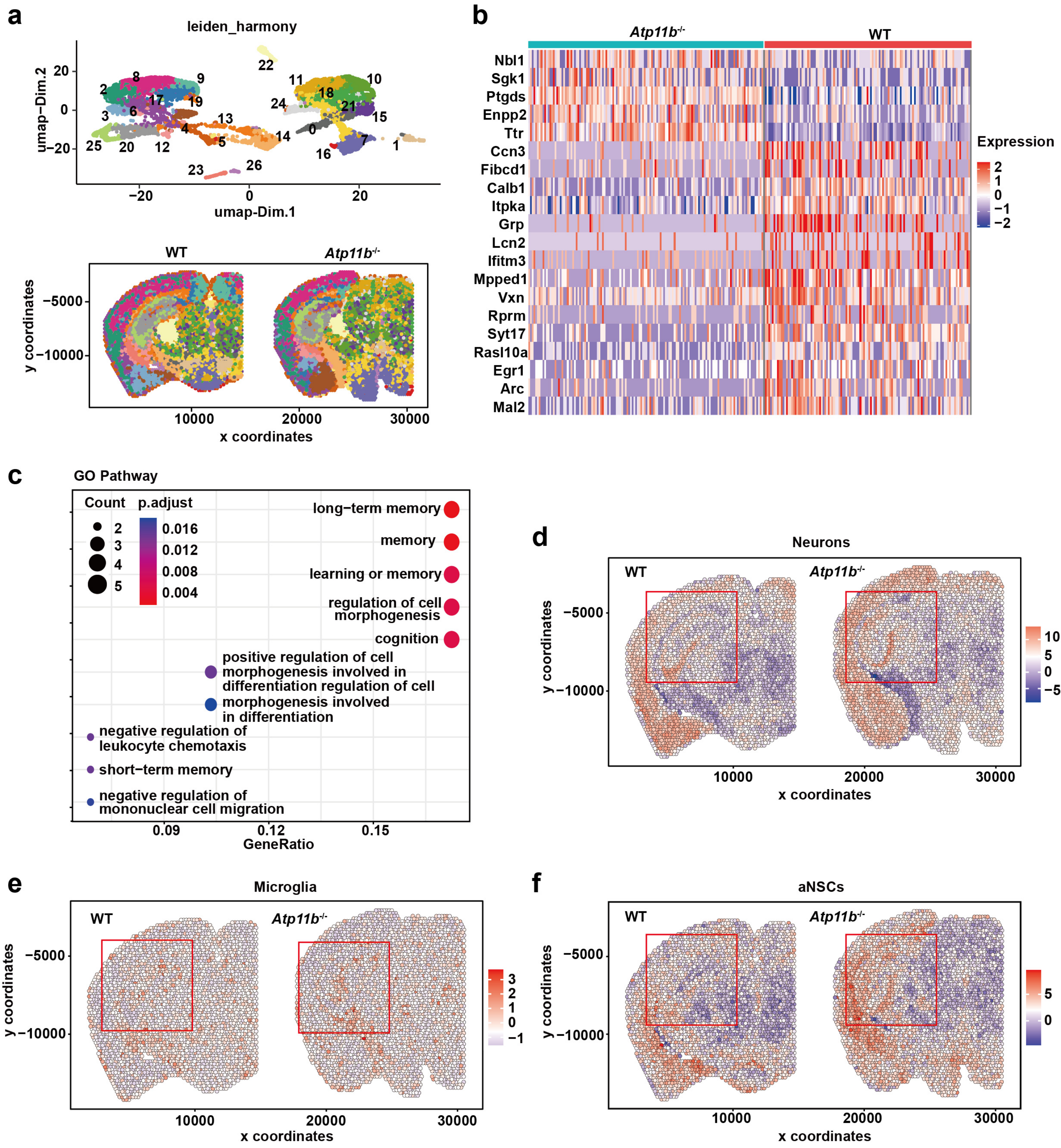
a
leiden_harmony
umap−Dim.2
umap−Dim.1
20
0
−20
−20
0
20
0 1 2 3 4 5 6 7 8 9 10 11 12 13 14 15 16 17 18 19 20 21 22 23 24 25 26
WT
Atp11b-/-
y coordinates
−5000
−10000
10000
20000
30000
x coordinates
b
Atp11b-/-
WT
Nbl1
Sgk1
Ptgds
Enpp2
Ttr
Ccn3
Fibcd1
Calb1
Itpka
Grp
Lcn2
Ifitm3
Mpped1
Vxn
Rprm
Syt17
Rasl10a
Egr1
Arc
Mal2
Expression
2
1
0
−1
−2
c
GO Pathway
Count
2
3
4
5
p.adjust
0.016
0.012
0.008
0.004
long−term memory
memory
learning or memory
regulation of cell morphogenesis
cognition
positive regulation of cell morphogenesis involved in differentiation
regulation of cell morphogenesis involved in differentiation
negative regulation of leukocyte chemotaxis
short−term memory
negative regulation of mononuclear cell migration
0.09
0.12
0.15
GeneRatio
d
Neurons
WT
Atp11b-/-
y coordinates
−5000
−10000
10000
20000
30000
x coordinates
10
5
0
−5
e
Microglia
WT
Atp11b-/-
y coordinates
−5000
−10000
10000
20000
30000
x coordinates
3
2
1
0
−1
f
aNSCs
WT
Atp11b-/-
y coordinates
−5000
−10000
10000
20000
30000
x coordinates
5
0

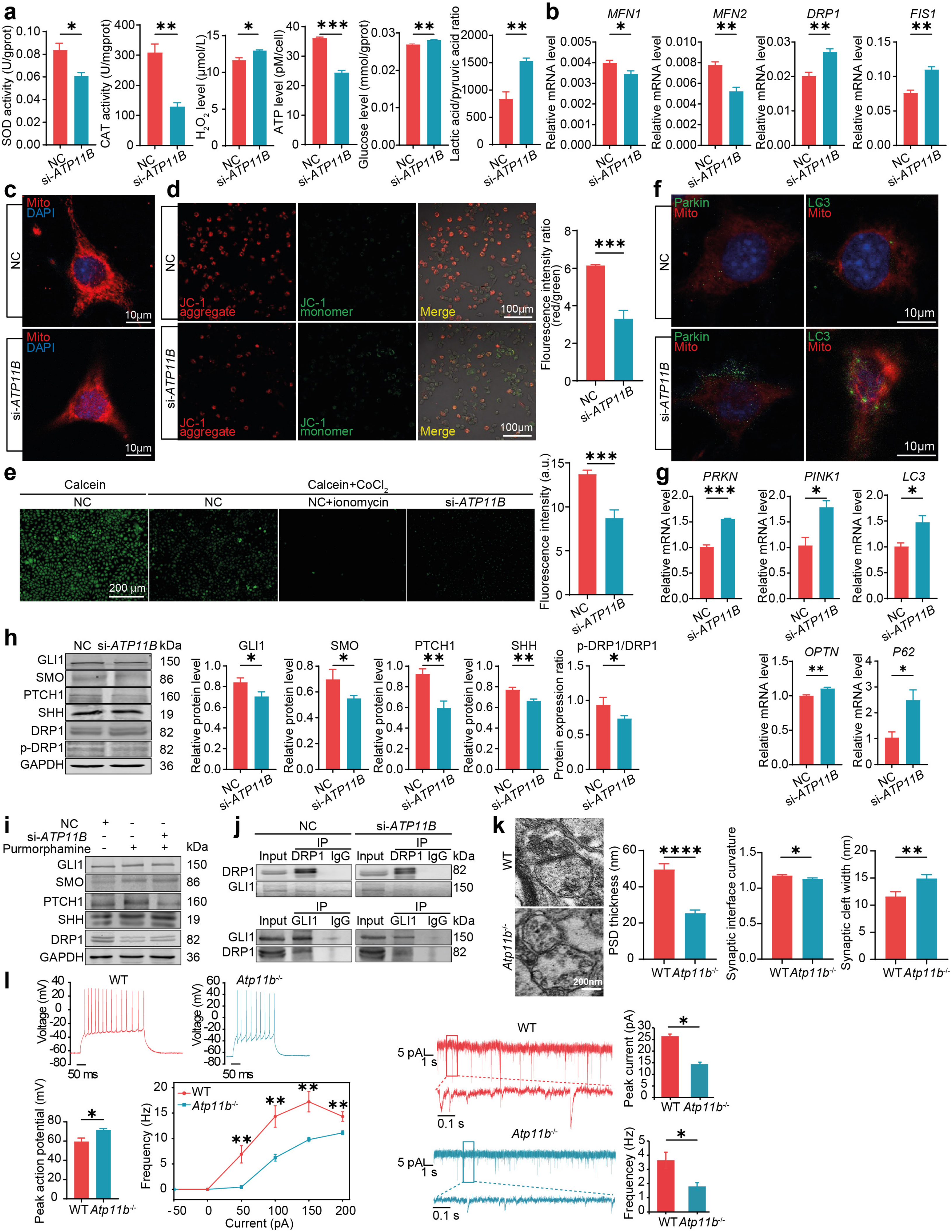
a
SOD activity (U/gprot)
0.10
0.08
0.06
0.04
0.02
0.00
*
CAT activity (U/mgprot)
400
300
200
100
0
**
H_2O_2 level (μmol/L)
15
10
5
0
*
ATP level (pM/cell)
40
30
20
10
0
***
Glucose level (mmol/gprot)
0.03
0.02
0.01
0.00
**
Lactic acid/pyruvic acid ratio
2000
1500
1000
500
0
**
NC
si-ATP11B
b
MFN1
*
MFN2
**
DRP1
**
FIS1
**
Relative mRNA level
0.005
0.004
0.003
0.002
0.001
0.000
0.010
0.008
0.006
0.004
0.002
0.000
0.03
0.02
0.01
0.00
0.15
0.10
0.05
0.00
NC
si-ATP11B
c
Mito
DAPI
NC
si-ATP11B
10μm
d
NC
si-ATP11B
JC-1 aggregate
JC-1 monomer
Merge
100μm
Flourescence intensity ratio (red/green)
8
6
4
2
0
***
NC
si-ATP11B
f
Parkin
Mito
LC3
Mito
NC
si-ATP11B
10μm
e
Calcein
Calcein+$CoCl_2$
NC
NC
NC+ionomycin
si-ATP11B
200 μm
Fluorescence intensity (a.u.)
15
10
5
0
***
NC
si-ATP11B
g
PRKN
***
PINK1
*
LC3
*
Relative mRNA level
2.0
1.5
1.0
0.5
0.0
OPTN
**
P62
*
1.5
1.0
0.5
0.0
4
3
2
1
0
NC
si-ATP11B
h
NC
si-ATP11B
kDa
GLI1 150
SMO 86
PTCH1 160
SHH 19
DRP1 82
p-DRP1 82
GAPDH 36
GLI1
*
SMO
*
PTCH1
**
SHH
**
p-DRP1/DRP1
*
Relative protein level
1.0
0.8
0.6
0.4
0.2
0.0
Protein expression ratio
1.5
1.0
0.5
0.0
NC
si-ATP11B
i
NC + - -
si-ATP11B - - +
Purmorphamine - + +
kDa
GLI1 150
SMO 86
PTCH1 160
SHH 19
DRP1 82
GAPDH 36
j
NC
si-ATP11B
IP
Input DRP1 IgG
Input DRP1 IgG
kDa
DRP1 82
GLI1 150
Input GLI1 IgG
Input GLI1 IgG
kDa
GLI1 150
DRP1 82
k
WT
Atp11b-/-
200nm
PSD thickness (nm)
60
40
20
0
****
Synaptic interface curvature
1.5
1.0
0.5
0.0
*
Synaptic cleft width (nm)
20
15
10
5
0
**
WT
Atp11b-/-
l
WT
Voltage (mV)
40
20
0
-20
-40
-60
-80
50 ms
Atp11b-/-
60
40
20
0
-20
-40
-60
-80
50 ms
Peak action potential (mV)
80
60
40
20
0
*
WT
Atp11b-/-
WT
Atp11b-/-
Frequency (Hz)
20
15
10
5
0
**
**
**
**
-50
0
50
100
150
200
Current (pA)
WT
5 pA
1 s
0.1 s
Peak current (pA)
30
25
20
15
10
5
0
*
WT
Atp11b-/-
Atp11b-/-
5 pA
1 s
0.1 s
Frequencey (Hz)
5
4
3
2
1
0
*
WT
Atp11b-/-

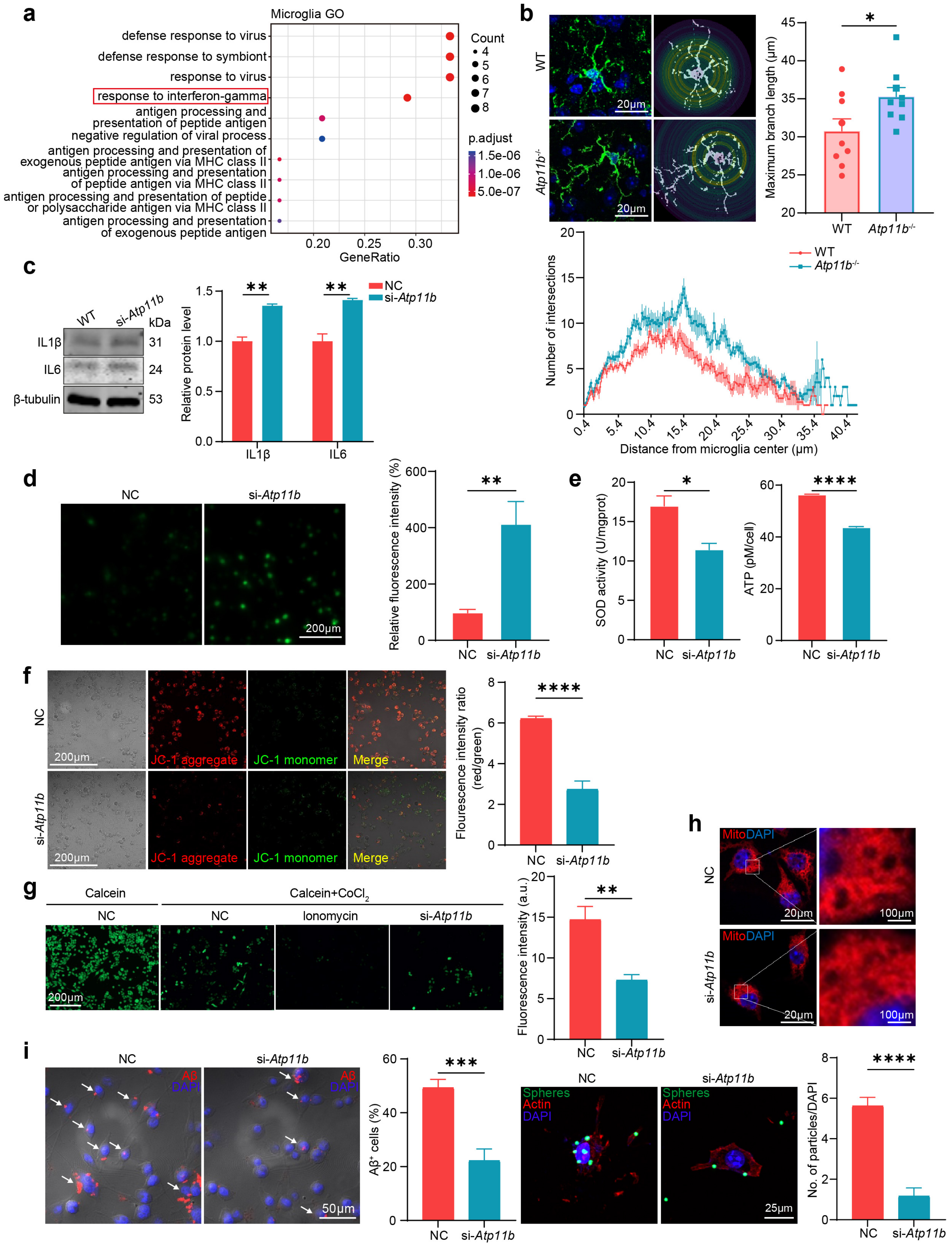
a
Microglia GO
defense response to virus
defense response to symbiont
response to virus
response to interferon-gamma
antigen processing and presentation of peptide antigen
negative regulation of viral process
antigen processing and presentation of exogenous peptide antigen via MHC class II
antigen processing and presentation of peptide antigen via MHC class II
antigen processing and presentation of peptide or polysaccharide antigen via MHC class II
antigen processing and presentation of exogenous peptide antigen
0.20
0.25
0.30
GeneRatio
Count
4
5
6
7
8
p.adjust
1.5e-06
1.0e-06
5.0e-07
b
WT
Atp11b-/-
20μm
20μm
*
Maximum branch length (μm)
45
40
35
30
25
20
WT
Atp11b-/-
Number of intersections
20
15
10
5
0
0.4
5.4
10.4
15.4
20.4
25.4
30.4
35.4
40.4
Distance from microglia center (μm)
WT
Atp11b-/-
c
WT
si-Atp11b
kDa
IL1β
31
IL6
24
β-tubulin
53
Relative protein level
1.5
1.0
0.5
0.0
**
**
NC
si-Atp11b
IL1β
IL6
d
NC
si-Atp11b
200μm
Relative fluorescence intensity (%)
600
400
200
0
**
NC
si-Atp11b
e
SOD activity (U/mgprot)
20
15
10
5
0
*
NC
si-Atp11b
ATP (pM/cell)
60
40
20
0
****
NC
si-Atp11b
f
NC
si-Atp11b
200μm
JC-1 aggregate
JC-1 monomer
Merge
200μm
JC-1 aggregate
JC-1 monomer
Merge
Flourescence intensity ratio (red/green)
8
6
4
2
0
****
NC
si-Atp11b
g
Calcein
Calcein+CoCl2
NC
NC
Ionomycin
si-Atp11b
200μm
Fluorescence intensity (a.u.)
20
15
10
5
0
**
NC
si-Atp11b
h
NC
si-Atp11b
Mito DAPI
20μm
100μm
Mito DAPI
20μm
100μm
i
NC
si-Atp11b
Aβ
DAPI
Aβ
DAPI
50μm
Aβ+ cells (%)
60
40
20
0
***
NC
si-Atp11b
NC
si-Atp11b
Spheres
Actin
DAPI
Spheres
Actin
DAPI
25μm
No. of particles/DAPI
8
6
4
2
0
****
NC
si-Atp11b

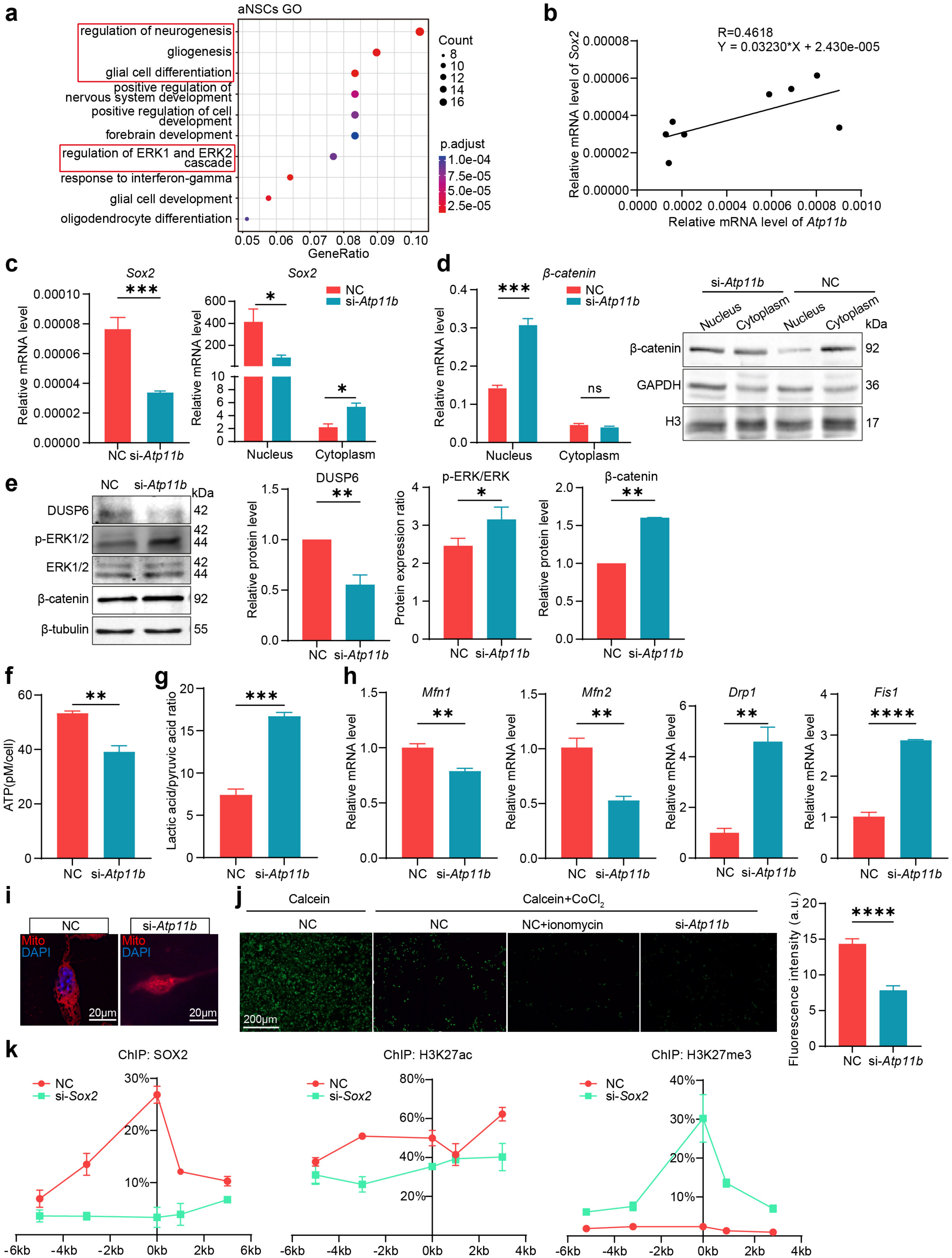
a
aNSCs GO
regulation of neurogenesis
gliogenesis
glial cell differentiation
positive regulation of nervous system development
positive regulation of cell development
forebrain development
regulation of ERK1 and ERK2 cascade
response to interferon-gamma
glial cell development
oligodendrocyte differentiation
0.05 0.06 0.07 0.08 0.09 0.10
GeneRatio
Count
8
10
12
14
16
p.adjust
1.0e-04
7.5e-05
5.0e-05
2.5e-05
b
R=0.4618
Y = 0.03230*X + 2.430e-005
Relative mRNA level of Sox2
0.00008
0.00006
0.00004
0.00002
0.00000
0.0000 0.0002 0.0004 0.0006 0.0008 0.0010
Relative mRNA level of Atp11b
c
Sox2
***
Relative mRNA level
0.00010
0.00008
0.00006
0.00004
0.00002
0.00000
NC si-Atp11b
Sox2
NC
si-Atp11b
*
*
600
400
200
10
8
6
4
2
0
Nucleus
Cytoplasm
d
β-catenin
***
ns
NC
si-Atp11b
Relative mRNA level
0.4
0.3
0.2
0.1
0.0
Nucleus
Cytoplasm
si-Atp11b
NC
Nucleus
Cytoplasm
Nucleus
Cytoplasm
kDa
β-catenin 92
GAPDH 36
H3 17
e
NC si-Atp11b kDa
DUSP6 42
p-ERK1/2 42 44
ERK1/2 42 44
β-catenin 92
β-tubulin 55
DUSP6
**
Relative protein level
1.5
1.0
0.5
0.0
NC si-Atp11b
p-ERK/ERK
*
Protein expression ratio
4
3
2
1
0
NC si-Atp11b
β-catenin
**
Relative protein level
2.0
1.5
1.0
0.5
0.0
NC si-Atp11b
f
**
ATP(pM/cell)
60
40
20
0
NC si-Atp11b
g
***
Lactic acid/pyruvic acid ratio
20
15
10
5
0
NC si-Atp11b
h
Mfn1
**
Relative mRNA level
1.5
1.0
0.5
0.0
NC si-Atp11b
Mfn2
**
Relative mRNA level
1.5
1.0
0.5
0.0
NC si-Atp11b
Drp1
**
Relative mRNA level
6
4
2
0
NC si-Atp11b
Fis1
****
Relative mRNA level
4
3
2
1
0
NC si-Atp11b
i
NC
si-Atp11b
Mito
DAPI
20μm
Mito
DAPI
20μm
j
Calcein
Calcein+CoCl$_2$
NC
NC
NC+ionomycin
si-Atp11b
200μm
****
Fluorescence intensity (a.u.)
20
15
10
5
0
NC si-Atp11b
k
ChIP: SOX2
NC
si-Sox2
30%
20%
10%
-6kb -4kb -2kb 0kb 2kb 4kb 6kb
ChIP: H3K27ac
NC
si-Sox2
80%
60%
40%
20%
-6kb -4kb -2kb 0kb 2kb 4kb
ChIP: H3K27me3
NC
si-Sox2
40%
30%
20%
10%
-6kb -4kb -2kb 0kb 2kb 4kb

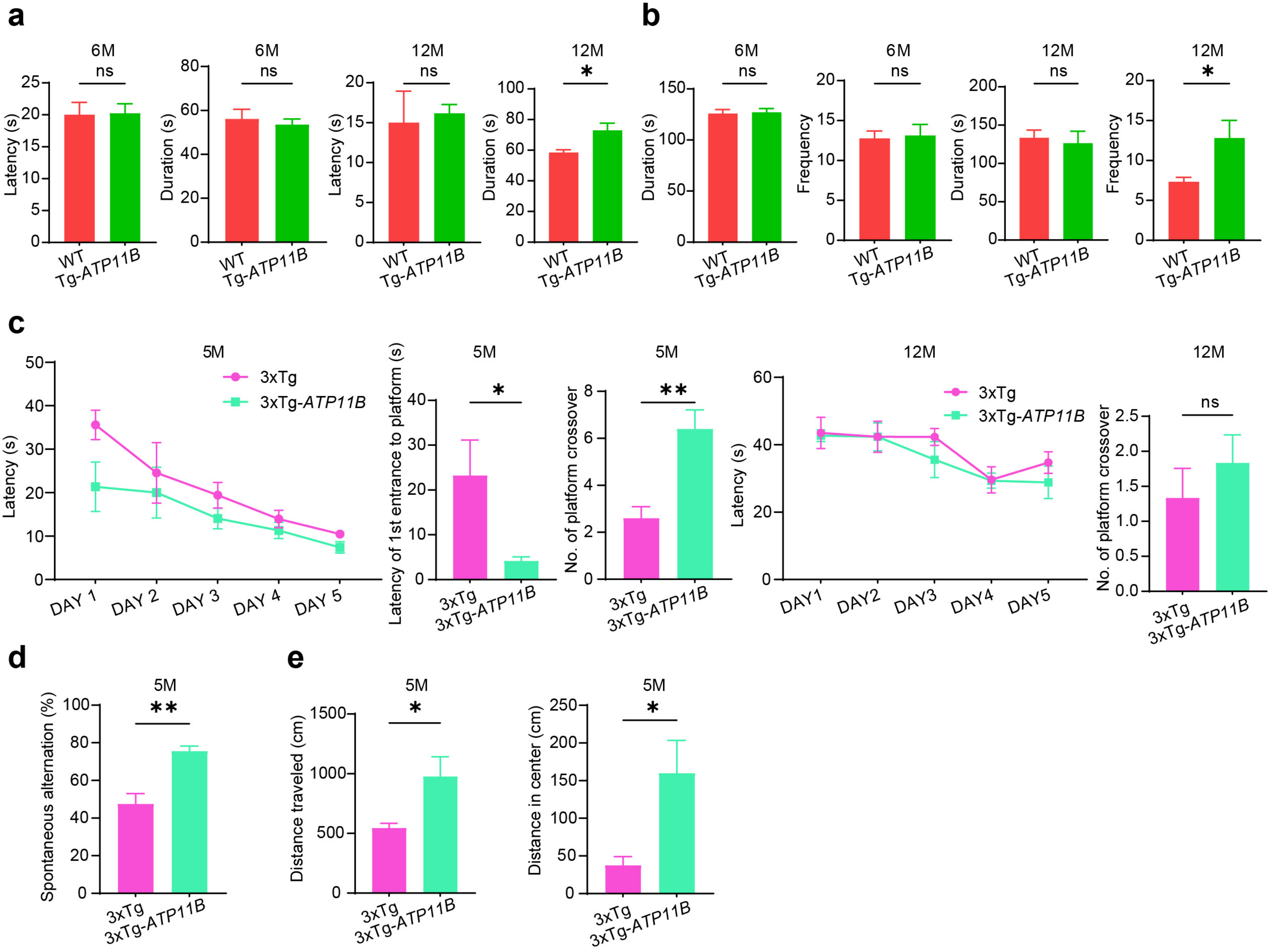
a
6M
ns
Latency (s)
25
20
15
10
5
0
WT
Tg-ATP11B
6M
ns
Duration (s)
80
60
40
20
0
WT
Tg-ATP11B
12M
ns
Latency (s)
20
15
10
5
0
WT
Tg-ATP11B
12M
*
Duration (s)
100
80
60
40
20
0
WT
Tg-ATP11B
b
6M
ns
Duration (s)
150
100
50
0
WT
Tg-ATP11B
6M
ns
Frequency
20
15
10
5
0
WT
Tg-ATP11B
12M
ns
Duration (s)
200
150
100
50
0
WT
Tg-ATP11B
12M
*
Frequency
20
15
10
5
0
WT
Tg-ATP11B
c
5M
3xTg
3xTg-ATP11B
Latency (s)
50
40
30
20
10
0
DAY 1
DAY 2
DAY 3
DAY 4
DAY 5
5M
*
Latency of 1st entrance to platform (s)
40
30
20
10
0
3xTg
3xTg-ATP11B
5M
**
No. of platform crossover
8
6
4
2
0
3xTg
3xTg-ATP11B
12M
3xTg
3xTg-ATP11B
Latency (s)
60
40
20
0
DAY1
DAY2
DAY3
DAY4
DAY5
12M
ns
No. of platform crossover
2.5
2.0
1.5
1.0
0.5
0.0
3xTg
3xTg-ATP11B
d
5M
**
Spontaneous alternation (%)
100
80
60
40
20
0
3xTg
3xTg-ATP11B
e
5M
*
Distance traveled (cm)
1500
1000
500
0
3xTg
3xTg-ATP11B
5M
*
Distance in center (cm)
250
200
150
100
50
0
3xTg
3xTg-ATP11B

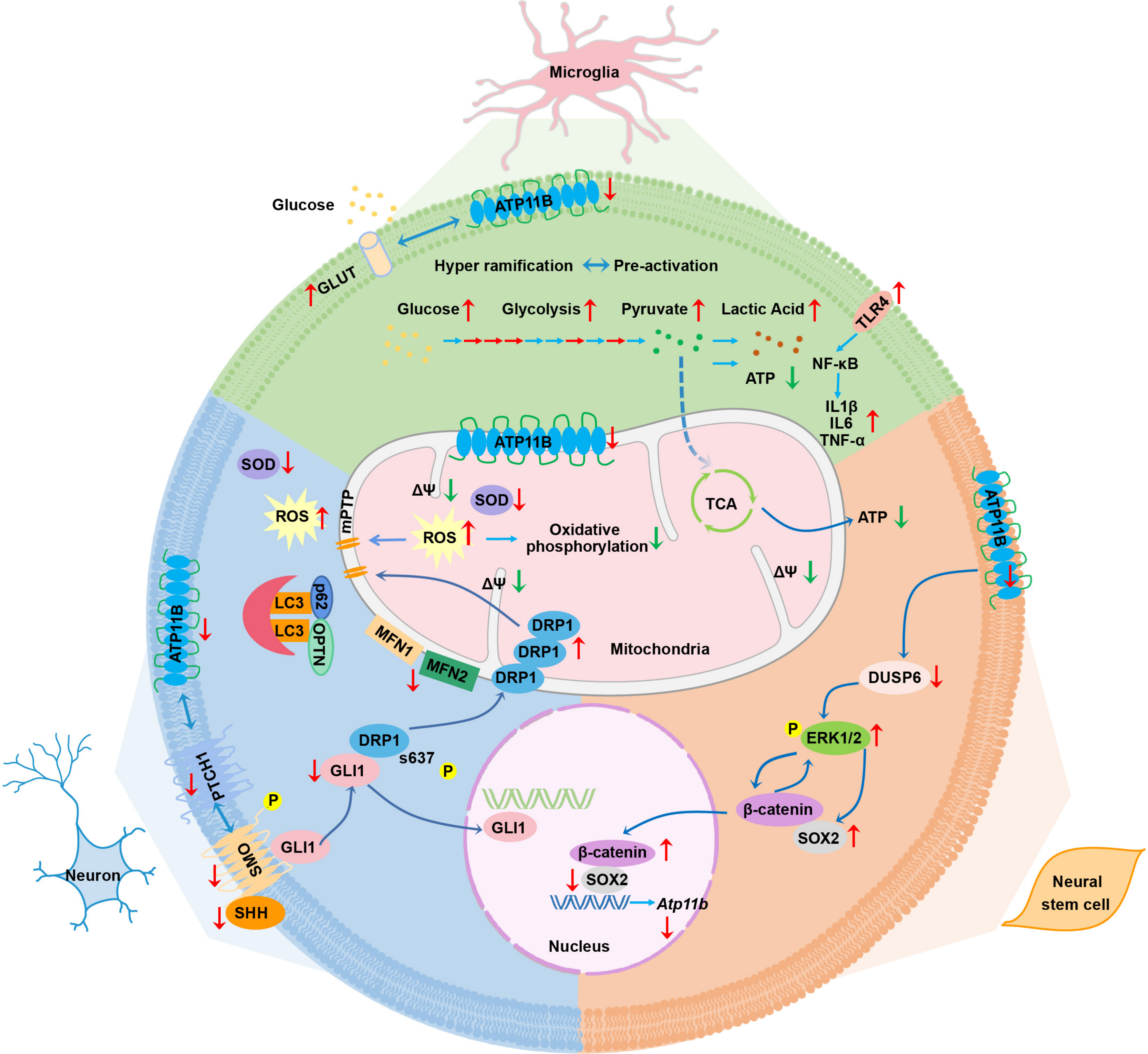
Microglia
Glucose
ATP11B
GLUT
Hyper ramification
Pre-activation
Glucose
Glycolysis
Pyruvate
Lactic Acid
TLR4
NF-κB
ATP
IL1β
IL6
TNF-α
ATP11B
SOD
ROS
mPTP
ΔΨ
SOD
ROS
Oxidative phosphorylation
TCA
ATP
ΔΨ
ΔΨ
ATP11B
LC3
LC3
p62
OPTN
MFN1
MFN2
DRP1
DRP1
DRP1
Mitochondria
ATP11B
DUSP6
P
ERK1/2
β-catenin
SOX2
DRP1
s637
P
GLI1
PTCH1
P
SMO
GLI1
SHH
Neuron
GLI1
β-catenin
SOX2
Atp11b
Nucleus
Neural stem cell

Supplementary Information for

ATP11B-related Mitochondrial Dysfunction Serves as an Early Alert of Alzheimer's Disease

Jiao Wang[1,10], Shibo Zhang[1,10], Qian Li[2,5,6,7,10], Ruiqi Sun[1,10], Wenxin Qi[1,10], Naijun Dong[1,10], Chengshang Lyu[3], Xiaoping Liu[3], Hao Wu[1], Jianxin Zhou[1], Hongwei Shi[1], Cuiping Liu[1], Junyi Zhuang[1], Peiru Wu[1], Lin Huang[1], Jintao Gong[2,5,6], Shuaijing Ma[2,5,6], Di Li[2,5,6], Xingyan An[1,5,6], Wanwei Zhao[1], Xuanting Liu[1], Qin Han[2,5,6], Rongjia Zhu[2,5,6], Shihua Wang[2,5,6], Hongling Li[2,5,6], Jing Li[2,5,6], Tieqiao Wen[1], Evelyne Bischof[8,9], Luonan Chen[3,4,*], and Robert Chunhua Zhao[1,2,5,6,*]

***Correspondence:**
zhaochunhua@ibms.pumc.edu.cn
lnchen@sibs.ac.cn

This file includes:
Supplementary Figures 1 to 6
Supplementary Tables 1, 2

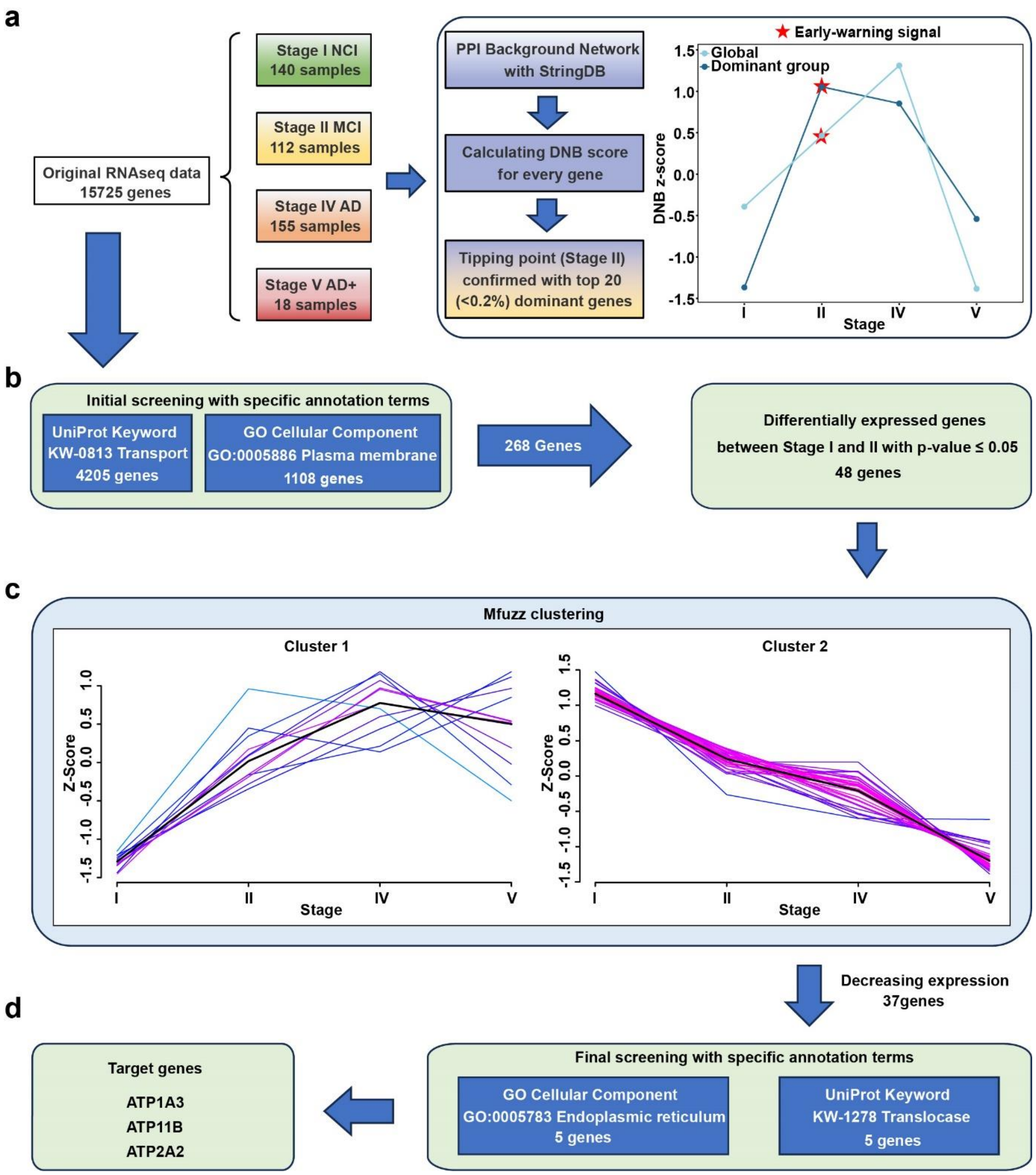

Supplementary Fig.1 The flowchart of AD pre-disease stage identification and tipping point gene screening. a, The identification of the tipping point of AD onset. The samples were divided into four subgroups according to the clinical classification of the subjects. A total of 15725 genes were analyzed via the l-DNB method to identify the critical stage before AD develops. The pre-disease stage is highlighted with red stars. **b,** The initial screening of DEGs between stage I (healthy control) and stage II (pre-disease stage). The genes overlapping with those associated with two annotation terms (KW-0813, GO:0005886) and showing alterations in expression between stage I and stage II were selected. **c,** The Mfuzz clustering of candidates from (**b**) to separate genes with distinct expression patterns. The black line in each figure represents the mean of z-transformed expression values. **d,** The final screening of tipping point genes for AD onset. The genes in cluster 2 of (**c**) were screened by overlapping with those associated with two additional annotation terms (KW-1278, GO:0005783), leading to the identification of 3 final candidate genes.

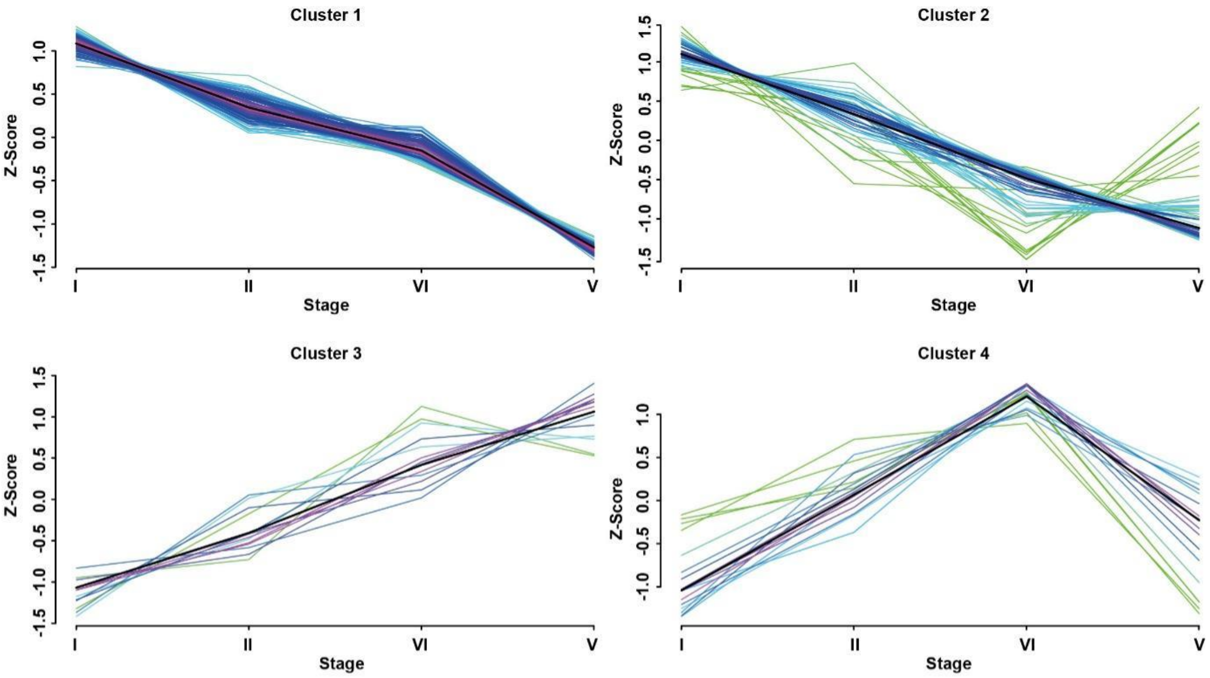

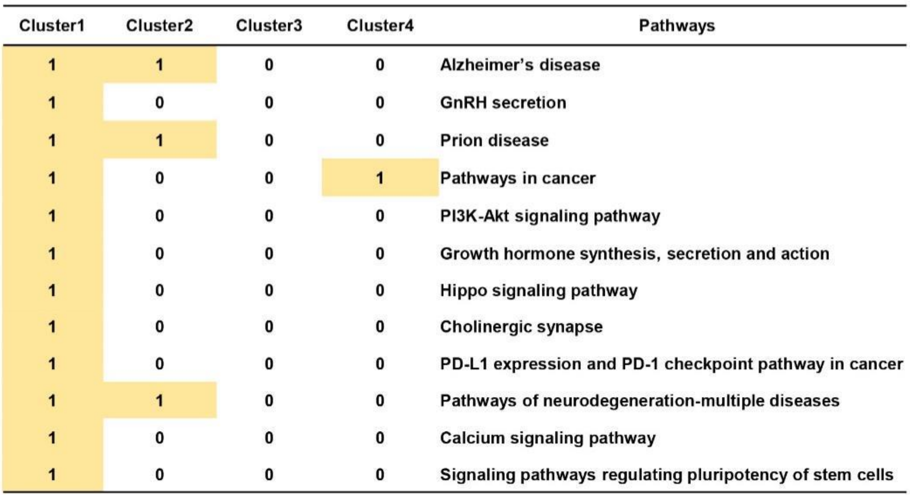

Cluster1	Cluster2	Cluster3	Cluster4	Pathways
1	1	0	0	Alzheimer's disease
1	0	0	0	GnRH secretion
1	1	0	0	Prion disease
1	0	0	1	Pathways in cancer
1	0	0	0	PI3K-Akt signaling pathway
1	0	0	0	Growth hormone synthesis, secretion and action
1	0	0	0	Hippo signaling pathway
1	0	0	0	Cholinergic synapse
1	0	0	0	PD-L1 expression and PD-1 checkpoint pathway in cancer
1	1	0	0	Pathways of neurodegeneration-multiple diseases
1	0	0	0	Calcium signaling pathway
1	0	0	0	Signaling pathways regulating pluripotency of stem cells

Supplementary Fig. 2 Expression patterns of genes in ATP11B-centered PPI network and their pathway enrichment highlights. The genes screened from the AD RNAseq dataset and centered around ATP11B in the PPI network were classified into 4 clusters based on their expression trends. The black line in each line chart represents the mean of z-transformed expression values. 1 and 0 mean the genes are enriched or not enriched in specific KEGG pathways listed, respectively.

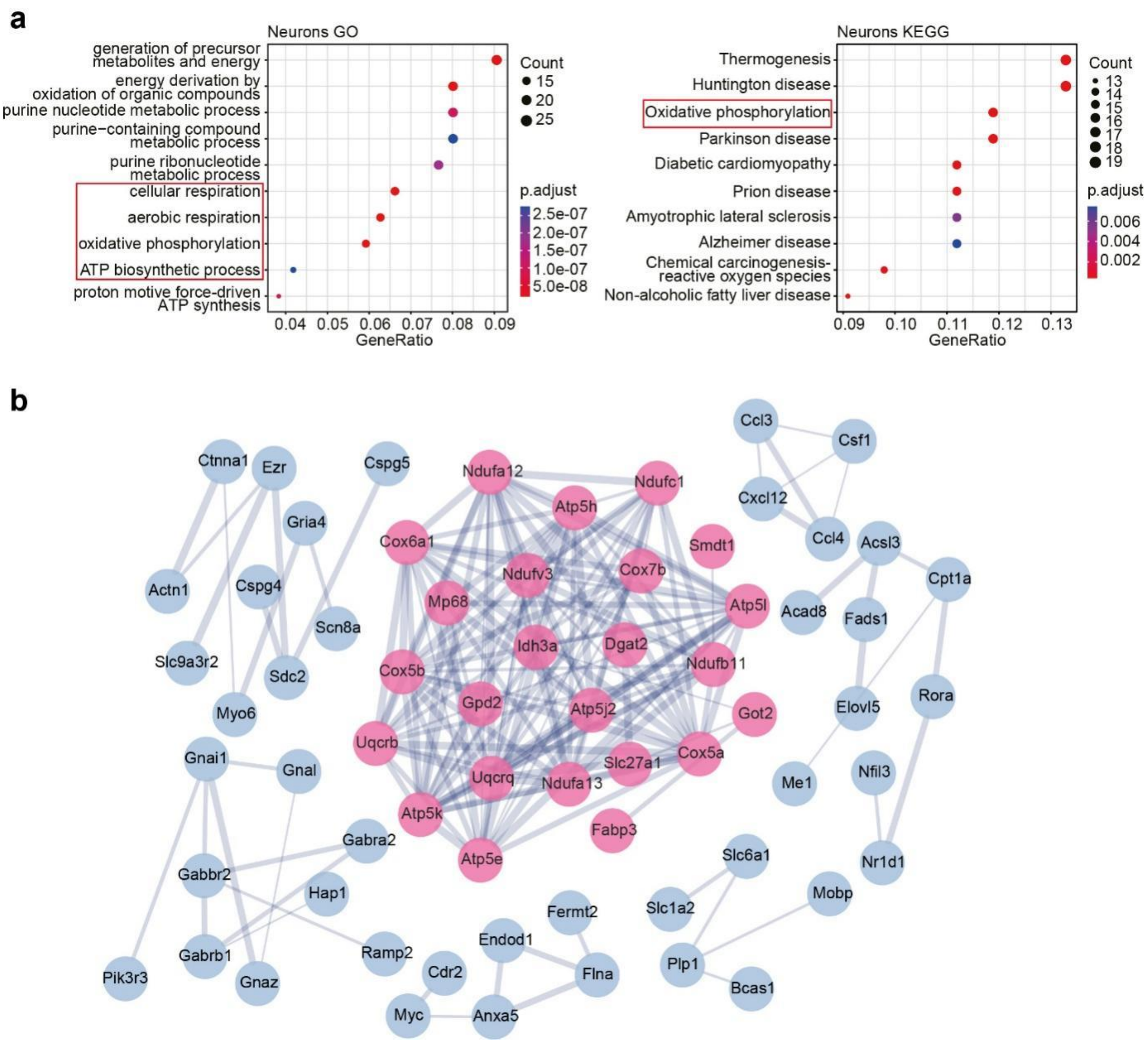

Supplementary Fig. 3 The functional enrichment analyses and PPI network of ATP11B deficiency-induced DEGs in mouse hippocampal neurons. a, GO and KEGG analyses of DEGs in neurons between the hippocampi of *Atp11b*$^{-/-}$ and wild-type mice. The red rectangles highlight pathways related to energy metabolism. **b,** The PPI network of DEGs in neurons between the hippocampi of *Atp11b*$^{-/-}$ and wild-type mice. The pink and blue colors indicate interaction numbers of ≥4 or <4 respectively. The thickness of the lines connecting interacting proteins corresponds to the interaction score.

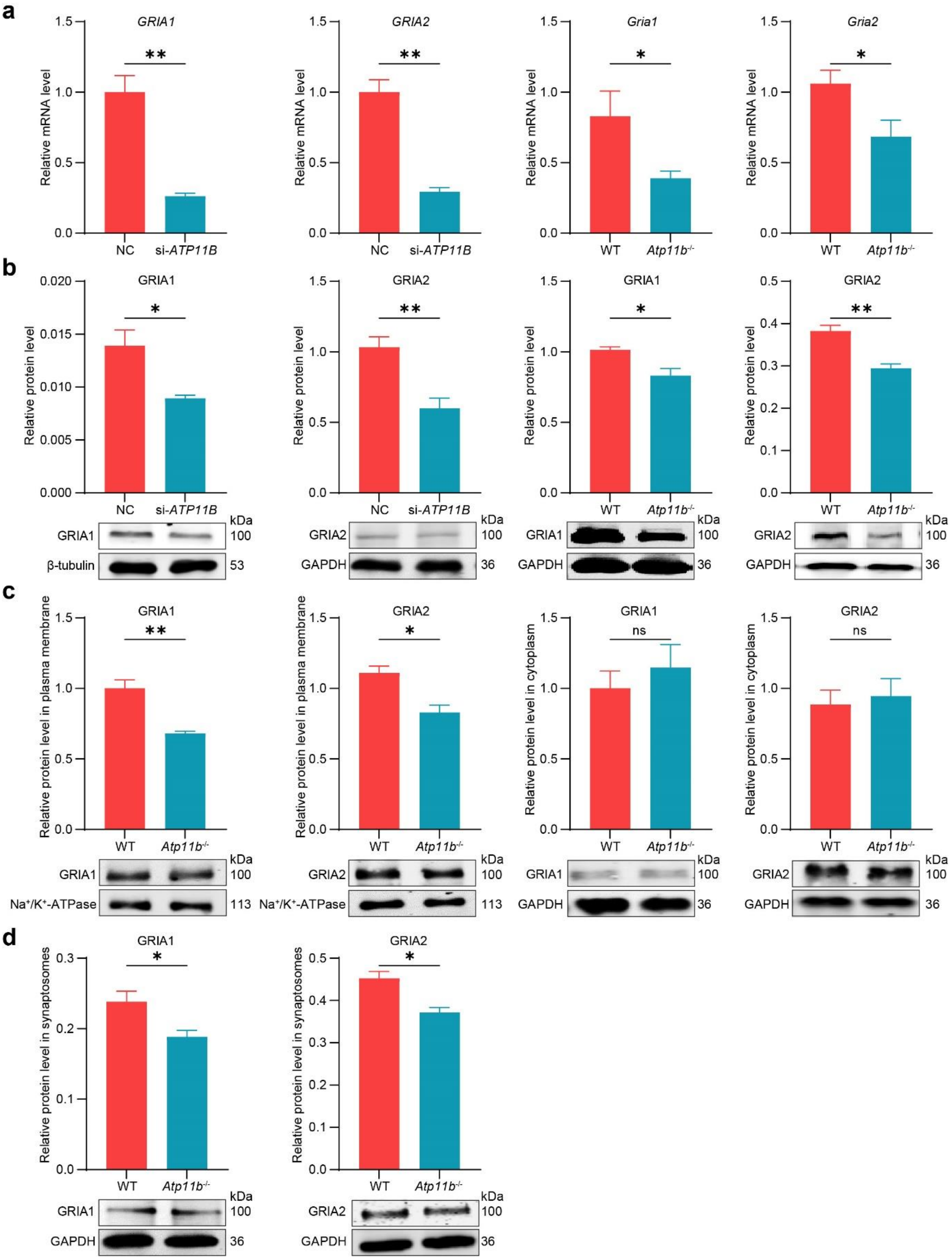

Supplementary Fig. 4 ATP11B is involved in AMPAR trafficking. a, b, Quantification of mRNA levels of *GRIA1*/*Gria1* and *GRIA2*/*Gria2* in *ATP11B*-silenced SH-SY5Y cells,*Atp11b*$^{-/-}$ mouse hippocampus and respective controls. **c, d** Quantification and representative western blots of GRIA1 and GRIA2 in the plasma membrane, cytoplasm (**c**) and synaptosomes (**d**) of hippocampal cells in wild-type and *Atp11b*$^{-/-}$ mice. Data in bar charts are represented as mean ± s.e.m. Unpaired two-tailed t-test, $n \geq 3$ batches of cells or $n \geq 3$ mice, *$P<0.05$, **$P<0.01$. ns, not significant; NC, negative control; WT, wild-type.

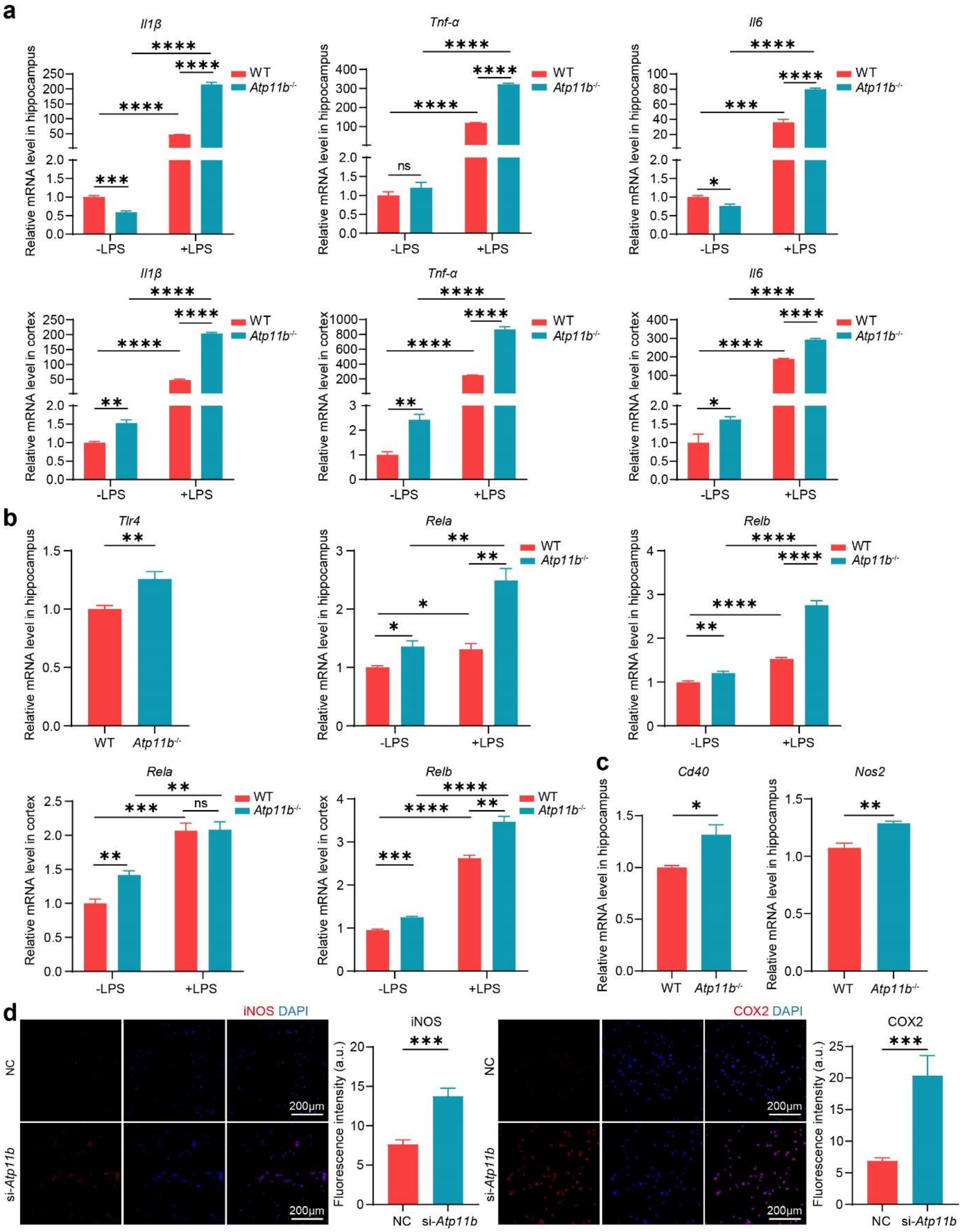

Supplementary Fig. 5 ATP11B deficiency results in pro-inflammatory responses in microglia. a-c, Quantification of mRNA levels of *Il1β*, *Tnf-α*, *Il6* (**a**), *Tlr4*, *Rela*, *Relb* (**b**), *Cd40* and *Nos2* (**c**) in the hippocampus or cortex of wild-type or *Atp11b*$^{-/-}$ mice without or with LPS induction. **d,** Representative confocal images of iNOS and COX2, and quantification of their protein levels in *Atp11b*-silenced BV2 and control cells. The fluorescence intensity normalized against the background noise indicates the protein level.

Scale bar: 200 µm. Data in bar charts are represented as mean ± s.e.m. Unpaired two-tailed t-test, (**a-c**) *n*≥3 mice, (**d**) *n*≥5 ROIs. **P*<0.05, ***P*<0.01, ****P*<0.001, *****P*<0.0001. ns, not significant; WT, wild-type; NC, negative control.

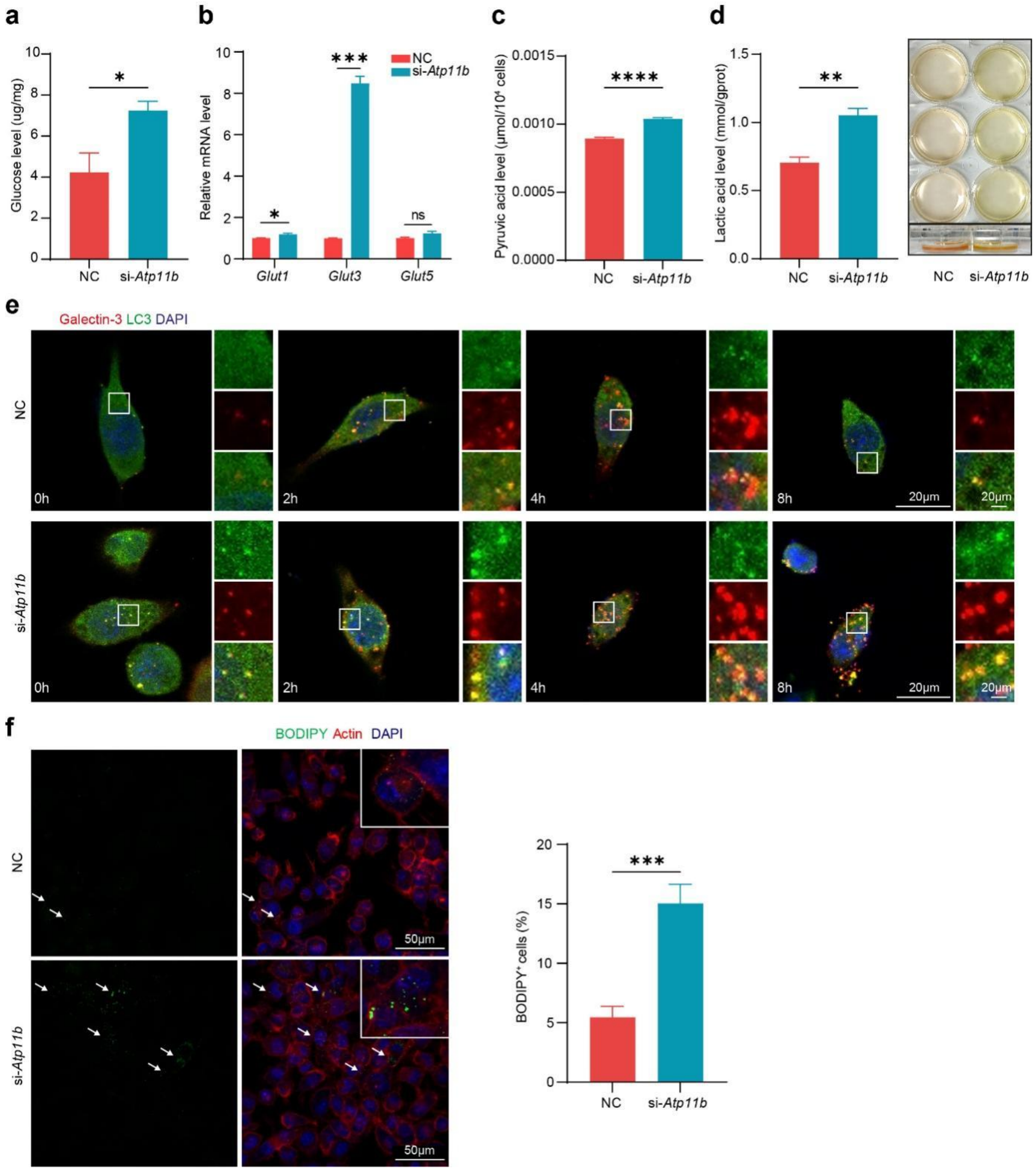

Supplementary Fig. 6 ATP11B deficiency causes energy metabolic imbalance, lysosomal disintegrity and lipid accumulation in microglia. a-d, Quantification of glucose levels (**a**), mRNA levels of *Glut1*, *Glut3* and *Glut5* (**b**), pyruvic acid levels (**c**) and lactic acid levels (**d**) in *Atp11b*-silenced BV2 and control cells. The photo in (**d**) shows that the PH of the culture media of *Atp11b*-silenced BV2 cells is more acidic (yellowish) than that of the control cells. **e,** Representative confocal microscopy images and quantification of lysosomal repair capacity in *Atp11b*-silenced BV2 and control cells. Damaged lysosomes are shown by the double labeling of Galectin-3 (red) and LC3 (green). Scale bar: 20 μm. **f,** Representative confocal microscopy images and quantification of lipid accumulation in

Atp11b-silenced BV2 and control cells. The intracellular lipid level is shown by the percentage of BODIPY-positive cells. The white arrows indicate cells containing lipid droplets. Scale bar: 50 μm. Data in bar charts are represented as mean ± s.e.m. Unpaired two-tailed t-test, (**a-d**) *n*=≥3 batches of cells, (**f**) *n*≥6 ROIs. **P*<0.05, ***P*<0.01, ****P*<0.001, *****P*<0.0001. ns, not significant; NC, negative control.

Supplementary Table 1 Classification of an AD RNAseq dataset.

COGDX			BRAAK		Stage
Score	**Characteristic**	**Number of subjects**	**Score**	**Number of subjects**	
1	NCI: no cognitive impairment	140	0	5	I
			1	22	
			2	15	
			3	52	
			4	40	
			5	6	
			6	0	
2	MCI: mild cognitive impairment	112	0	1	II
			1	2	
			2	15	
			3	41	
			4	42	
			5	11	
			6	0	
4	AD: Alzheimer’s, without any other medical condition that causes cognitive impairment	155	0	0	IV
			1	5	
			2	6	
			3	32	
			4	50	
			5	57	
			6	5	
5	AD+: Alzheimer’s with other medical condition(s) that cause(s) cognitive impairment	18	0	0	V
			1	0	
			2	1	
			3	6	
			4	7	
			5	4	
			6	0	

The classification of the AD cases was based on the final consensus cognitive status (the COGDX score) and the severity of neurofibrillary tangles (the BRAAK score). The subjects in stages III (MCI+, MCI with another condition causing CI, *n*=6) and VI (other dementia, no clinical evidence of AD, *n*=12) were excluded because of small sample size and lack of clinical evidence of AD respectively.

Supplementary Table 2 Mitochondrial protein-encoding genes identified by l-DNB.

Gene name	Identity	Function[a]
MT-ATP6	Subunit of ATP synthase (complex V)	Contributes to ATP synthase activity, rotational mechanism, and proton transport
MT-ATP8		
MT-CO1	Subunit of cytochrome c oxidase (complex IV)	Contributes to the activity of complex IV
MT-CO2		Contributes to the activity of complex IV
MT-CO3		Involved in the assembly of complex IV
MT-ND1	Subunit of NADH:ubiquinone oxidoreductase (complex I)	Essential for the catalytic activity and assembly of complex I
MT-ND2		Essential for the catalytic activity and assembly of complex I
MT-ND3		Essential for the catalytic activity of complex I
MT-ND4		Essential for the catalytic activity and assembly of complex I
MT-ND4L		Predicted to be involved in complex I activity and electron transport
MT-ND5		Essential for the catalytic activity and assembly of complex I
MT-CYB	Cytochrome b, component of ubiquinol-cytochrome c reductase (complex III)	Contributes to the generation of a proton gradient
COX7A2L	Likely a regulatory subunit of cytochrome c oxidase (complex IV)	Possibly involved in the assembly of mitochondrial respiratory supercomplex
COX8A	Subunit of cytochrome c oxidase (complex IV)	Possibly involved in the regulation of complex IV activity
COX11	Cytochrome c oxidase copper chaperone	Required for the assembly of complex IV
COX10	Cytochrome c oxidase assembly factor heme A: farnesyltransferase	Required for the expression and maturation of functional complex IV
COX18	Mitochondrial membrane insertase	Required for the assembly, stability, and activity of complex IV
NDUFAF5	Arginine hydroxylase	Involved in the assembly of complex I
SCO1	Copper metallochaperone	Essential for the maturation of complex IV and copper homeostasis

[a] The information of gene functions was summarized from https://www.ncbi.nlm.nih.gov/gtr/genes/ and https://www.nextprot.org/